HL-TWiM empirical model of high-latitude upper thermospheric winds

Manbharat S. Dhadly[1,2], John T. Emmert[1], Douglas P. Drob[1], Mark G. Conde[3], Anasuya Aruliah[4], Eelco Doornbos[5], Gordon G. Shepherd[6], Qian Wu[7], Jonathan J. Makela[8], Rick J. Niciejewski[9], Changsup Lee[10], Geonhwa Jee[10], and Aaron J. Ridley[9]

[1]Space Science Division, Naval Research Laboratory, Washington DC, USA
[2]Department of Physics and Astronomy, George Mason University, Virginia, USA
[3]Geophysical Institute, University of Alaska Fairbanks, Alaska, USA
[4]Department of Physics and Astronomy, University College London, England
[5]Royal Netherlands Meteorological Institute - KNMI, The Netherlands
[6]Centre for Research in Earth and Space Science, York University, Canada
[7]High Altitude Observatory, UCAR, Colorado, USA
[8]Department of Electrical and Computer Engineering, University of Illinois at Urbana-Champaign, Illinois, USA
[9]Climate and Space Sciences and Engineering, University of Michigan, Ann Arbor, Michigan, USA
[10]Korea Polar Research Institute, Incheon, Korea

Key Points:

- We developed a comprehensive empirical model of high-latitude F region thermospheric winds (HL-TWiM).
- Universal Time variations in high-latitude winds are stronger in the Southern than Northern Hemisphere.
- HL-TWiM provides a necessary benchmark for validating new high-latitude wind observations and tuning first principal models.

Corresponding author: Manbharat Dhadly, manbharat.dhadly.ctr@nrl.navy.mil

Abstract

We present an empirical model of thermospheric winds (HL-TWiM - High-latitude Thermospheric Wind Model) which specifies F region high-latitude horizontal neutral winds as a function of day-of-year, latitude, longitude, local time, and geomagnetic activity. HL-TWiM represents the large-scale neutral wind circulation, in geomagnetic coordinates, for the given input conditions. The model synthesizes the most extensive collection to date of historical high-latitude wind measurements; it is based on statistical analyses of several decades of F region thermospheric wind measurements from 21 ground-based stations (Fabry-Perot Interferometers (FPIs) and Scanning Doppler Imaging FPIs (SDIs)) located at various northern and southern high latitudes and 2 space-based instruments (UARS WINDII and GOCE). The geomagnetic latitude and local time dependences in HL-TWiM are represented using Vector Spherical Harmonics (VSH), day-of-year and longitude variations are represented using simple harmonic functions, and the geomagnetic activity dependence is represented using quadratic B-splines. In this paper, we describe the HL-TWiM formulation and fitting procedures, and we verify the model against the neutral wind databases used in its formulation. HL-TWiM provides a necessary benchmark for validating new wind observations and tuning our physical understanding of complex wind behaviors. Results show stronger Universal Time (UT) variation in winds at southern than northern-high latitudes. Model-data intra-annual comparisons in this study show semi-annual oscillation (SAO) like behavior of GOCE winds, rarely observed before in wind data.

1 Introduction

The most dynamic effects of space weather in the near-Earth environment occur at high latitudes. At these latitudes, magnetosphere-ionosphere-thermosphere (MIT) interactions compose a dynamic, nonlinear, and closely coupled system, one in which thermospheric winds respond directly via ion drag to ionospheric plasma motions that are imposed by solar wind-magnetosphere interactions (e.g., Rees & Fuller-Rowell, 1989). The polar ionosphere and thermosphere act as an energy and particle sink for the magnetosphere. The energy dumped from the magnetosphere to the thermosphere-ionosphere (TI) system modifies the composition and dynamics of the thermosphere and ionosphere. Thermospheric neutral winds at high latitudes are a primary driver of transport and global redistribution of the energy and momentum deposited by the magnetosphere (e.g., Dhadly & Conde, 2017). They can lead to significant global disturbances in ionospheric and thermospheric weather by transporting high-latitude energy, momentum, and composition changes (e.g., Crowley, Emery, Roble, Carlson, & Knipp, 1989; Crowley, Emery, Roble, Carlson, Salah, et al., 1989; Strickland et al., 1999; Pallamraju, 2005). Recent observational studies (e.g., G. Shepherd & Shepherd, 2018; M. Shepherd et al., 2019) suggest that wind reversal occurring in the auroral zone plays an important role in the vertical coupling of thermosphere and ionosphere. Thermospheric and ionospheric weather are of considerable practical and operational interest for satellite operators, navigators, and communicators. Thus, high-latitude thermospheric winds are an imperative aspect of the coupled MIT system and understanding their behavior is critical for operational space weather applications.

Despite decades of research, observational understanding of the dynamic nature of thermospheric circulation at middle to polar latitudes and its systematic response to various heliospheric and magnetospheric forcing is still mainly qualitative and lags the corresponding understanding of ionospheric dynamics in many ways. This is largely due to historically sparse neutral wind observations (e.g., Meriwether, 2006). Unlike ionospheric drift monitoring by SuperDARN radars (e.g., Chisham et al., 2007), it is currently not possible to construct an instantaneous picture of large-scale high-latitude thermospheric winds. No single observational data set provides comprehensive space-time coverage of the high-latitude wind system. However, over the past two decades, historical observational databases have grown sufficiently to permit at least a meaningful statistical analysis of large-scale high-latitude horizontal winds. Thus, empirical characterization of high-latitude winds based on their statistical behavior provides an invaluable resource for scientific applications (e.g., Drob et al., 2015). Even though physics-based models are getting better with increasing complexity, it is extremely valuable to have tools like observationally derived climatologies that represent actual data as they serve as a necessary benchmark for validating new databases and tuning our physical understanding of complex wind behaviors.

In this paper, we statistically analyze several decades of measurements of Earth's F region thermospheric horizontal winds and apply an empirical approach to advance our understanding of neutral circulation at high latitudes. Specifically, we develop a parametric representation of high-latitude neutral winds as a function of day-of-year (DOY), latitude, longitude, local time, and geomagnetic activity in geomagnetic coordinates. There is no other empirical model, except the Horizontal Wind Model (HWM14) (Drob et al., 2015), that characterizes the large-scale behavior of high-latitude neutral winds as a function of these arguments. However, HWM14 is limited at high latitudes in that its global winds are based on geographic coordinates. Previous studies (e.g., Hays et al., 1984; Richmond, 1995; Emmert et al., 2008) have shown that neutral circulation at high latitudes is better organized in geomagnetic coordinates; this is because ionospheric plasma motions are naturally organized by the Earth's magnetic field and ion drag is one of the primary drivers of thermospheric circulation at high latitudes. Thus, for a better characterization of the high-latitude neutral winds, data assimilation in geomagnetic coordinates is a natural choice.

Several statistical studies of F region northern and southern high-latitude thermospheric winds have been conducted in the past using ground-based and space-based wind data (e.g., Rees et al., 1983; Rees & Fuller-Rowell, 1989; Meriwether et al., 1988; R. W. Smith et al., 1988, 1994; Aruliah et al., 1991, 1996; Hernandez et al., 1991; Hernandez & Roble, 2003; Emmert, Hernandez, et al., 2006; Emmert, Faivre, et al., 2006; Wu et al., 2008; Lee et al., 2017). However, many of them present a local view of the thermosphere and are more focused on the Northern Hemisphere (NH). A relatively broad view is necessary to understand the global effect of high-latitude thermosphere dynamics and interactions with the ionosphere. Large-scale studies of high-latitude winds are rare (e.g., Richmond et al., 2003; Emmert et al., 2008; Förster et al., 2011; Förster & Cnossen, 2013; Dhadly & Conde, 2017; Dhadly et al., 2018). Southern high-latitude studies are even more scant due to the harsh conditions and the effort required to maintain an instrument on a long-term basis. Until now, the data sample sizes were not enough for any definitive climatological conclusions to be drawn. A major fraction of prior research has been focused on the northern high latitudes because of the lower effort required to make ground-based measurements and coordinated ground and space-based campaigns. Richmond et al. (2003) used the extensive upper thermospheric wind database generated by the UARS WINDII instrument to obtain statistical wind patterns for different Interplanetary Magnetic Field (IMF) conditions. Förster et al. (2011) and Förster and Cnossen (2013) used CHAMP cross-track measurements to statistically analyze the high-latitude neutral wind patterns in both Northern and Southern Hemispheres (SH). Emmert et al. (2008) emphasized a different approach for high latitudes than HWM14 and calculated global disturbed winds (Disturbance Wind Model (DWM07)) by subtracting out quiet-time patterns; DWM07 predicts perturbation as a function of magnetic latitude (MLAT) and magnetic local time (MLT) by combining global wind data from seven ground-based and two space-based instruments. Recently, Dhadly et al. (2017, 2018) combined northern high-latitude wind measurements from eight ground-based and three space-based instruments to investigate the seasonal and geomagnetic activity dependence of large-scale neutral circulation. But we are not aware of any investigations that have yet resolved the full day-of-year and magnetic longitude (as well as Universal Time (UT)) dependence of winds at high latitudes.

Leveraging the ideas from earlier studies, we have developed a new empirical characterization of upper thermospheric winds (which is HL-TWiM) for both the northern and southern high latitudes; it provides a valuable specification of F region neutral winds as a function of day-of-year, latitude, longitude, local time, and geomagnetic conditions in magnetic coordinates. This empirical formulation is based on the available measurements from an armada of diverse instruments. The underlying mathematical foundation of HL-TWiM is based on the DWM07 model (Emmert et al., 2008), but is more advanced. DWM07 calculates disturbance wind vectors as a function of MLAT, MLT, and Kp, while HL-TWiM calculates the total wind vector as a function of DOY, MLAT, MLON, MLT, and Kp. Further, the UT dependence of high-latitude neutral circulation has been rarely studied. Although UT is not an argument in HL-TWiM, its relation to magnetic longitude and magnetic local time allows the model to be used for this purpose. In addition, HL-TWiM includes unique and new southern hemispheric wind observations that have not been explored in any previous empirical/observational studies. The recent installation of new FPIs and SDIs in Antarctica has widely extended our spatio-temporal coverage of wind measurements over Antarctica that was not available before.

The effectiveness of the driving forces at high-latitude varies with latitude and hence creates wind regimes as a function of latitude. Thus, we have divided high latitudes into three sectors: polar (80-90 MLAT), auroral (60-80 MLAT), and middle latitudes (45-60 MLAT). We have used the same NH wind databases discussed in Dhadly et al. (2017, 2018), with the addition of new European FPIs (Longyearbyen, Kiruna, and Sodankyla). So, here we will focus the discussion more on the new FPIs and southern hemispheric wind databases as some of them have never been available or published before.

2 Observational Wind Data

HL-TWiM is based on long-term thermospheric F region neutral wind observations (altitudes between 210 km and 320 km) obtained from 2 space-based and 21 ground-based instruments located at various northern and southern high latitudes above 45-degree magnetic latitude. Table 1 highlights these instruments and their key characteristics (such as locations, data coverage, and descriptive references). Out of these 21 ground-based wind databases, 16 are from narrow field of view FPIs and 5 are from wide field of view SDIs. The space-based databases included are GOCE and UARS WINDII. The locations of observations of ground-based stations both in geographic and geomagnetic coordinates are shown in Figure 1.

The space-based instruments provide global wind coverage but with limited temporal resolution for any given location. On the other hand, the ground-based instruments measure winds at high temporal cadence, but with limited spatial sampling. Thus, we combined the ground-based and space-based data to get the extended spatial and temporal coverage. The extent of data coverage at northern and southern high-latitude for each season is shown in Figure 2. Almost all of the available high-latitude daytime wind measurements are from the space-based instruments. Although this study is focused only on magnetic latitudes poleward of 45, wind fits are calculated for a full sphere using vector spherical harmonics, and the data equatorward of 45 magnetic latitude (GOCE and WINDII) act to anchor those fits.

The NH ground-based stations included here are: Thule FPI (TH FPI), Resolute Bay FPI (RB FPI), Søndre Strømfjord FPI (SS FPI), Longyearbyen (LY FPI), Toolik Lake SDI (TL SDI), Poker Flat SDI (PF SDI), Kiruna (KR FPI), Sodankyla (SK FPI), Millstone Hill FPI (MH FPI), Peach Mountain FPI (PM FPI), and Urbana FPI (UR FPI). The comprehensive details of these NH wind databases are presented in Dhadly et al.

(2017, 2018), except for the European sector FPIs (LY FPI, KR FPI, and SK FPI). The details of European sector FPIs can be found in Aruliah and Griffin (2001); Griffin et al. (2002, 2004); Aruliah et al. (2004, 2005). Wind databases such as LY, KR, SK, UR, PM, and MH FPI are in the form of line-of-sight (LOS) winds, whereas others are reduced to the zonal and meridional components of the horizontal vector wind.

So far only few (e.g., Richmond et al., 2003; Emmert et al., 2008; Drob et al., 2015, etc.) have studied the large-scale neutral wind circulation at southern high latitudes by combining data from ground-based and space-based instruments. DWM07 (Emmert et al., 2008) used only two southern high-latitude ground-based stations, and provides no seasonality and longitude information of winds, while HWM14 is formulated in geographic coordinates and used four southern high-latitude stations. For the SH, this study used data from 10 ground-based stations (SDIs and FPIs). These stations are: Arrival Heights FPI (AH FPI), Jang Bogo FPI (JB FPI), McMurdo SDI (MM SDI), South Pole FPI (SP FPI), South Pole SDI (SD SDI), Mawson SDI (MW SDI), Halley FPI (HA FPI), Palmer FPI (PL FPI), King Sejong FPI (KS FPI), and Mount John FPI (MJ FPI). Their detailed description, observational modes, and data reduction techniques can be found in the references cited in Table 1. Out of these southern instruments, four instruments (KS FPI, JB FPI, SD SDI, and MM SDI) have been recently installed and data from three of them (KS FPI, SD SDI, and MM SDI) have not been published before. The hardware, observational modes, and data reduction technique of the SDIs installed at South Pole and McMurdo (SD SDI and MM SDI) are similar to the PF SDI discussed in (Conde & Smith, 1995; Dhadly et al., 2015; Dhadly & Conde, 2017). KS FPI operation and instrumentation are similar to the FPI discussed in (Wu et al., 2004).

The data recorded by SDIs and FPIs are based on measuring the Doppler shift in red line (630 nm) nightglow emissions. 630 nm emissions have a vertical profile with the peak emission altitude centered around 220–250 km. Thus, the measured wind is an altitudinal integration of the winds weighted by the emission intensity. During daytime, green line (557.7 nm) optical emissions come from a wide range of altitudes from MLT region to the upper thermosphere, but at nighttime they are limited to the lower thermosphere (∼90-130km). WINDII used green line optical emissions to measure daytime winds from MLT to the upper thermosphere; nighttime winds were measured using red line optical emissions from the F region thermosphere (G. Shepherd et al., 2012). WINDII nighttime winds (red line) were not observed on a routine basis as they were outside the UARS objectives, but nevertheless a significant dataset was acquired. Following the discussion in Dhadly et al. (2017, 2018), we have selected data in the altitude range of 210–320 km assuming no statistically significant height dependence in wind climatology in the selected altitude range (as discussed by Killeen et al. (1982); Wharton et al. (1984); Emmert et al. (2002)).

GOCE cross-track winds between altitudes 224 km and 295 km are derived using the onboard accelerometer measurements (Doornbos et al., 2013). It was in a near-polar, sun-synchronous orbit, crossing the equator at dawn and dusk periods. The majority of the GOCE data are centered on the solar terminator.

The major challenge of the effort here is to combine these disparate neutral wind databases into a coherent picture while overcoming their spatio-temporal sampling limitations. As enacted in Dhadly et al. (2017, 2018), to prevent one set of measurements dominating the statistical wind fitting, we apply de-weighting to the dense datasets such as GOCE and SDIs by selecting 5% of their data randomly. This subjective, ad hoc approach was also used in the production of other major empirical models, including all versions of HWM (Drob et al., 2015) and of the Mass Spectrometer Incoherent Scatter radar (MSIS) temperature and composition models (Picone et al., 2002).

The available data span 1983 to 2016 with daily 10.7 cm solar radio flux ($F10.7$) varying between 60 solar flux units (sfu) and 400 sfu (1sfu = 10^{-22} Wm^{-2}Hz^{-1}). The dependence of high-latitude winds on solar flux is not well understood; therefore, to avoid any possibility of high solar flux conditions skewing HL-TWiM wind fitting, we have only used data when $F10.7 < 150$.

3 Data Bias and Correction

The construction of HL-TWiM is based on data from the instruments operating independently at different locations and rarely cross-calibrated (e.g., Dhadly et al., 2015). Thus, this study also serves as a platform to cross-compare the overlapping datasets.

Dhadly et al. (2017, 2018) found no major biases among the northern high-latitude stations and satellites except GOCE, and a possible statistical solution for removing apparent bias was adopted. The most evident discrepancies were removed from GOCE northern high-latitude data by estimating a general GOCE empirical bias profile based on the data climatology from other stations. Similarly, in this study, we found no consistent major biases among southern high-latitude databases except GOCE (details discussed below).

The GOCE dataset is unique and important. The GOCE orbit is fixed in local time, thus the cross-contamination between local time and seasonal variations are minimal. Even though the GOCE winds are limited to only dawn-dusk periods, it is the only dataset that provides a comprehensive overview of the seasonal variation with high spatio-temporal resolution. GOCE winds are cross-track winds (Doornbos, 2011) derived indirectly using a model of the satellite geometry, aerodynamics, and measurement of acceleration from the onboard accelerometer (Doornbos et al., 2010). Discrepancies between GOCE and other data could be associated with the approximations (such as satellite geometry and gas-surface interaction) used in satellite aerodynamics model (Doornbos et al., 2010; Visser et al., 2018, 2019). Any small variation in estimates of gas-satellite surface interaction and the way satellite geometry pointed with respect to wind flow can introduce such errors in wind estimates (Visser et al., 2018, 2019). We cannot exclude that part of the discrepancy could also be attributed to errors in the processing of the airglow-based wind measurements from the FPI, SDI and WINDII instruments. An extensive investigation, taking into account errors in both measurement techniques, would be required to fully reconcile the discrepancies.

Dhadly et al. (2018) included GOCE data version 1.3. In the present study, we have used updated GOCE data version 1.5. The updated GOCE bias profile for northern high latitudes based on (Dhadly et al., 2018) using GOCE data version 1.3 is shown in Figure 3. In this study, we found similar discrepancies in GOCE data at southern high latitudes and applied the bias correction technique used in (Dhadly et al., 2018). WINDII provides extensive coverage of the southern-high-latitude as a function of magnetic latitude and magnetic local time as shown in Figure S1. This luxury of large spatio-temporal coverage was not available in the NH. So, in the SH, we have used WINDII to remove the most discernable bias trend from GOCE winds. The steps followed in this procedure, similar to the Dhadly et al. (2018) procedure are:

1. Using quiet-time ($Kp < 3$) southern (MLAT<-45) WINDII data, produce a quiet-time baseline wind climatology (VSH - order 12 and degree 3) as a function of MLAT and MLT.
2. Evaluate WINDII baseline model winds from step 1 at the locations of GOCE quiet-time observations.
3. Bin and average quiet-time GOCE cross-track winds as a function of MLAT and MLT.
4. Bin and average the evaluated WINDII model winds from step 2 as a function of MLAT and MLT (same as step 3) and project them along the GOCE cross-track wind directions to calculate cross-track WINDII model winds.

5. Subtract binned and averaged WINDII model cross-track winds from the binned and averaged GOCE cross-track winds to compute the residual cross-track wind as a function of MLAT for several MLT bins (dawn and dusk MLT bins shown in Figure S2).
6. Although the bias profiles on dawnside and duskside have similar latitudinal profiles, they have different magnitudes. So, average duskside and dawnside residual profiles separately to obtain general bias profiles for each side as a function of MLAT, as shown in Figure 3 (bottom panel).
7. Subtract these bias profiles from the GOCE cross-track measurements to obtain corrected GOCE winds.

An example comparison between original GOCE, corrected GOCE, and WINDII cross-track winds is shown in Figure S3; it shows significant bias improvements in the GOCE cross-track winds. The average bias in uncorrected and corrected GOCE cross-track winds compared to WINDII is 92 m/s and 38 m/s, respectively. The root mean square difference between uncorrected GOCE and WINDII is 112 m/s, whereas it is 49 m/s between corrected GOCE and WINDII. Interestingly, despite the existence of bias in GOCE winds, GOCE uncorrected data and WINDII show similar latitudinal wind features (shown in Figure S3 here and Dhadly et al. (2018) Figure S7 and S8). The major motivation behind this bias removal operation is to make the best possible use of the GOCE data to guide wind fitting in regions where other data become sparse to none.

4 Model Formulation and Fitting

Similar to Emmert et al. (2008) and Dhadly et al. (2017, 2018), we developed a linear parametric representation of high-latitude winds using Vector Spherical Harmonic (VSH) functions for a full sphere as the core basis functions. This allows us to assimilate the single-component wind databases such as GOCE cross-track winds and FPI LOS winds. The neutral wind data are assimilated in Quasi-Dipole geomagnetic coordinates (Richmond, 1995; Emmert et al., 2010), which provide a better characterization of high-latitude wind behavior than geographic coordinates. Based on earlier studies (discussed above), we calculated VSH expansion coefficients up to degree 10 in magnetic latitude and order 3 in magnetic local time. As in Emmert et al. (2008), the geomagnetic activity dependence of winds is modeled using three quadratic B-spline functions shown in Figure 4. The Kp quadratic B-splines have nodes at {0, 2, 5, 6.5} and zero slope at Kp=0 and 6.5, and tapering after Kp >6.5. We tapered splines for Kp >6.5 compared to for Kp >8 in Emmert et al. (2008) because the addition of a day-of-year modulation of the Kp dependence further dilutes the available high-Kp data. These constraints provide needed robustness at the edges of the Kp domain where data are insufficient to reliably determine the coupled Kp-MLAT-MLT-day-of-year dependence. In addition to Kp, HL-TWiM includes day-of-year and magnetic longitude dependences, but they are not coupled with each other. We used annual and semi-annual harmonics to represent the day-of-year behavior of winds. The magnetic longitudinal dependence in winds is represented by the first harmonic (wave number 1). The complete mathematical formulation of HL-TWiM is given below:

$$\vec{U}(\lambda,\tau,d,\delta,Kp) = \sum_{k=0}^{2}\sum_{s=0}^{2}\sum_{n=1}^{10}\sum_{m=1}^{n} \vec{\psi}^1{}_{ksnm}(\lambda,\tau,d,Kp) + \sum_{n=1}^{10}\sum_{m=1}^{n} \vec{\psi}^2{}_{nm}(\lambda,\tau,\delta) \quad (1)$$

The $\vec{\psi^1}_{ksnm}(\lambda,\tau,d,Kp)$ and $\vec{\psi^2}_{nm}(\lambda,\tau,\delta)$ are give by:

$$\begin{aligned}\vec{\psi^1}_{ksnm}(\lambda,\tau,d,Kp) = N_k(Kp)\left[a^R_{ksnm}\vec{V}^R_{nm} + a^I_{ksnm}\vec{V}^I_{nm} + b^R_{ksnm}\vec{W}^R_{nm} + b^I_{ksnm}\vec{W}^I_{nm}\right]\cos(sd)\\ +N_k(Kp)\left[c^R_{ksnm}\vec{V}^R_{nm} + c^I_{ksnm}\vec{V}^I_{nm} + d^R_{ksnm}\vec{W}^R_{nm} + d^I_{ksnm}\vec{W}^I_{nm}\right]\sin(sd)\end{aligned} \tag{2}$$

$$\begin{aligned}\vec{\psi^2}_{nm}(\lambda,\tau,\delta) = \left[e^R_{nm}\vec{V}^R_{nm} + e^I_{nm}\vec{V}^I_{nm} + f^R_{nm}\vec{W}^R_{nm} + f^I_{nm}\vec{W}^I_{nm}\right]\cos(\delta)\\ +\left[g^R_{nm}\vec{V}^R_{nm} + g^I_{nm}\vec{V}^I_{nm} + h^R_{nm}\vec{W}^R_{nm} + h^I_{nm}\vec{W}^I_{nm}\right]\sin(\delta)\end{aligned} \tag{3}$$

323 where vector spherical harmonic basis functions ($\vec{V}_{nm}$ and $\vec{W}_{nm}$) are given by:

$$\vec{V}^R_{nm} = \left[+\frac{d\overline{P}_{nm}}{d\theta}\cos(m\omega\tau)\hat{e}_\theta - \frac{m}{\sin(\theta)}\overline{P}_{nm}\sin(m\omega\tau)\hat{e}_\phi\right]\frac{1}{\sqrt{n(n+1)}} \tag{4}$$

$$\vec{V}^I_{nm} = \left[-\frac{d\overline{P}_{nm}}{d\theta}\sin(m\omega\tau)\hat{e}_\theta - \frac{m}{\cos(\theta)}\overline{P}_{nm}\sin(m\omega\tau)\hat{e}_\phi\right]\frac{1}{\sqrt{n(n+1)}} \tag{5}$$

$$\vec{W}^R_{nm} = \left[-\frac{m}{\sin(\theta)}\overline{P}_{nm}\sin(m\omega\tau)\hat{e}_\theta - \frac{d\overline{P}_{nm}}{d\theta}\cos(m\omega\tau)\hat{e}_\phi\right]\frac{1}{\sqrt{n(n+1)}} \tag{6}$$

$$\vec{W}^I_{nm} = \left[-\frac{m}{\sin(\theta)}\overline{P}_{nm}\cos(m\omega\tau)\hat{e}_\theta + \frac{d\overline{P}_{nm}}{d\theta}\sin(m\omega\tau)\hat{e}_\phi\right]\frac{1}{\sqrt{n(n+1)}} \tag{7}$$

$$\overline{P}_{nm}(\theta) = \sqrt{\frac{(2n+1)(n-m)!}{2(n+m)!}}P_{nm}(\theta) \tag{8}$$

$$\theta = \frac{\pi}{2} - \lambda \tag{9}$$

where N_k are the Kp splines; k is the index of the Kp spline; s gives the order of harmonics used for seasonal variation; n and m are the order and degree of VSH fits for magnetic latitude and magnetic local time, respectively; and d, δ, λ, θ, τ represent day-of-year, magnetic longitude, magnetic latitude, magnetic colatitude, and magnetic local time, respectively. $P_{nm}(\theta)$ and $\overline{P}_{nm}(\theta)$ are the unnormalized and normalized associated Legendre functions, respectively; and $\hat{e}_\theta$ and $\hat{e}_\phi$ are the southward and eastward unit vectors. The vector functions $\vec{V}^R$, $\vec{V}^I$, $\vec{W}^R$, $\vec{W}^I$ are the real and imaginary parts of the irrotational (V) and solenoidal (W) complex vector spheric harmonic (VSH) functions. $\{a^R_{ksnm}$, a^I_{ksnm}, b^R_{ksnm}, b^I_{ksnm}, c^R_{ksnm}, c^I_{ksnm}, d^R_{ksnm}, d^I_{ksnm}, e^R_{nm}, e^I_{nm}, f^R_{nm}, f^I_{nm}, g^R_{nm}, g^I_{nm}, h^R_{nm}, $h^I_{nm}\}$ are the model fit coefficients ($=m_{fit}$). A total of 2176 model fit coefficients were calculated. In the model formulation (equation 1), when m>n VSH functions are zero. As presented in the mathematical formulation of HL-TWiM in equation 1, there is no coupling between longitudinal and Kp or day-of-year variability of winds. Other than that, all the model basis functions are fully coupled. The model fit coefficients m_{fit} are computed by minimizing the sum of squared differences between the wind measurements and corresponding model output component. Some of the datasets (such as GOCE, LY FPI, etc) are in the form of either line-of-sight (LOS) or cross-track measurements; in these cases, we minimize the sum of squared differences between the LOS wind measurements and corresponding component of the model vector. For datasets with available vector winds, the zonal and meridional components were treated as separate LOS winds as in Emmert et al. (2008) and Dhadly et al. (2017). A detailed discussion of avoiding singularities and ambiguities near the poles using VSH is given in Emmert et al. (2008).

It is important to note that, because this model is only for middle to polar latitudes (|MLAT| >45), the model parameters were estimated separately for the NH and SH.

The model script is written in FORTRAN-90. All the end user HL-TWiM FORTRAN-90 subroutines and coefficient files are available in a zipped package in the supporting information of this paper.

5 Model Validation and Discussion

In this section, we evaluate the HL-TWiM behavior by comparing its output against the constituent databases used in its formulation. This operation allows us to 1). compare model output with other databases as well as compare databases against each other where they overlap and 2). visualize any discrepancies that may exist among the databases. All the wind databases that exist for the F-region thermsphere at high latitudes are already included, thus there are virtually no independent databases available for independent validation, except a couple of balloon-borne FPI measurements from the HIWIND (High altitude Interferometer WIND experiment) (Wu, Knipp, Liu, Wang, Häggström, et al., 2019; Wu, Knipp, Liu, Wang, Varney, et al., 2019). We compared HL-TWiM with two days of HIWIND neutral wind measurements (DOY 177 and 176 of 2018) and the results are shown in Figure S4. This comparison of HL-TWiM with independent data demonstrates the constrained behavior of HL-TWiM in data scant regions.

5.1 Statistical Performance

We used bias (μ) and root mean square error (σ) as two statistical metrics to quantify the model performance, measuring the model fidelity, and goodness of fit. They are defined as:

$$\mu = \frac{1}{N}\sum_{i=1}^{N}(obs_i - model_i) \tag{10}$$

$$\sigma = \sqrt{\frac{\sum_{i=1}^{N}(obs_i - model_i)^2}{N}} \tag{11}$$

where N is the total number of observations, obs_i represent the observational data, and $model_i$ represent the estimated winds. Table 2 shows the bias and root mean square error for zonal, meridional, and cross-track winds. μ and σ are calculated for each station. In the table, HWM14 is included for reference. For μ and σ calculation, the winds from HL-TWiM and HWM14 are calculated at the locations of data. Note that these statistical metrics are calculated separately for geomagnetic zonal, meridional, and cross-track winds. In addition, these metrics show model performance at the locations where data is available. These metrics shown in Table 2 demonstrate a significant improvement in HL-TWiM winds over HWM14.

Note that for SP FPI, because of its location (the geographic south pole), the measured LOS winds are geographic meridional winds. However, because the SP FPI observation locations (refer to Figure 1) are at an elevation of 30 degree (∼86S), it is possible to roughly calculate horizontal vector winds. We followed Emmert, Faivre, et al.

(2006) and combined four look direction LOS wind measurements separated by 90 degree of longitude, assuming a constant wind field. For Table 2, we used LOS winds from 75E, 165E, 15W, and 105W and followed Emmert, Faivre, et al. (2006) to obtain vector winds from SP FPI measurements.

For the GOCE metrics in Table 2, first we calculated model vector winds at the locations of GOCE data and then projected the calculated vector winds along the GOCE cross-track directions.

5.2 Local Time Dependence and Seasonality

Figures 5 to 8 show observed and HL-TWiM winds (geomagnetic zonal and meridional) as a function of magnetic local time (hourly bins) at the magnetic latitudes at the FPI and SDI stations (with latitudinal and longitude coverage same as the extent of north-south and east-west observation locations of the station data) for various DOY bins. Each DOY bin covers 60 days. The DOY numbers shown on the right represent the centers of each DOY bin. For the most direct comparison between data and model, first the model was run at the space-time locations of observations, and then binned and averaged in the same way as the data (blue curve). The green and red curves represent WINDII daytime and nighttime winds at the station location (with latitudinal and longitude coverage same as the extent of north-south and east-west observation locations of the station), respectively. There are two subfigures for each station - one for quiet and other for active geomagnetic conditions. To check the robustness of the model at the locations of limited or no data availability, we also calculated the model winds on a regular space-time grid (shown as black curve) at the station locations with latitudinal and longitude coverage same as the extent of north-south and east-west observation locations of the station data. The model was run for each MLT hour at 10-day intervals. The error bars represent the estimated uncertainty of the mean in each bin calculated by dividing standard deviation by the square root of the number of days in the sample (Emmert et al., 2002; Emmert, Faivre, et al., 2006).

Overall, HL-TWiM and data morphology agree in both the hemispheres. Comparing zonal and meridional winds, the agreement between data and model is better for meridional winds. WINDII green line winds provided daytime wind coverage, whereas SDIs, FPIs, and WINDII red line winds provided nighttime wind coverage. That is why in the summer time, WINDII green line winds cover more local times than in winter.

At northern high latitudes, as shown in Figure 5, HL-TWiM zonal winds agree well with binned and averaged zonal winds from all other databases except SS FPI. SS FPI zonal winds show diurnal fluctuations that are not present in nearby stations (such as European FPIs) and are not well captured by the model. The differences between the SS FPI zonal winds and the model are up to $\sim$70 m/s and are largest under equinox conditions. Note that the model behavior at a location also depends on the other databases present in the vicinity of that location. This could be a reason for the discrepancy. Also, the discrepancies between model and WINDII zonal winds are stronger around this station than any others. However, no such discrepancies exist for meridional winds (Figure 6).

At southern high latitudes, AH FPI and MM SDI are at the same location. In geographic sense, JB FPI latitude is $\sim$3 degree lower than AH FPI and MM SDI, but magnetically all the three are located approximately at the same latitude (79.9S MLAT, see Figure 1). Figures 7 and 8 (first panel in each), show their wind comparisons. All three stations show similar diurnal variation in winds, but the magnitudes of their diurnal variations are different. JB zonal winds are strongest and AH zonal winds are weakest of all the three. On average in SH winter, JB and MM quiet-time zonal winds are $\sim$53 m/s and $\sim$29 m/s stronger than AH, respectively; JB and MM quiet-time meridional winds are ∼43 m/s and ∼17 m/s stronger than AH, respectively. Similar differences exist in model, JB, and MM winds as the model wind are closer to AH winds.

A discrepancy of ∼100 m/s between model and data zonal wind is present at MJ FPI location for active Kp, DOY bin 90, between 2200 and 0400 MLT (Figure 7). MJ FPI zonal winds in this bin are not consistent with the other neighboring DOY bins and neighboring latitude stations (such as PL, KS, and HA FPI). A similar discrepancy is present at MJ FPI, between WINDII red line winds and MJ FPI zonal winds (quiet KP, DOY bin 30, Figure 7). Based on the data from other neighboring space-time locations, the WINDII red line winds appear to be more realistic. A similar large discrepancy of ∼100 m/s is present between modeled and MM SDI active time zonal winds around 1900-2400 MLT.

In all the seasons, MJ, PL, and KS FPI combined with WINDII measurements show semidiurnal variation (∼50 m/s amplitude) in zonal winds, which is not as apparent in the NH stations around the same latitudes. At these stations, the semidiurnal behavior intensifies with geomagnetic activity. In the NH, semidiurnal behavior in zonal wind is strongest around auroral latitudes, in contrast to these SH mid-latitude stations.

The local time dependence of winds for northern and southern high-latitude show some interesting dependences on Kp. The effect of Kp on meridional winds appears to decrease with decreasing latitude (Figures 6 and 8). The effect of Kp on zonal winds at middle latitudes is comparable with high latitudes.

In addition, to quantify how the distribution of data (especially the large summer gaps) affects the uncertainty of the modeled average winds (at the model resolution), the supporting information includes contour plots of the estimated model uncertainty for two FPI stations – Thule and Poker Flat (Figure S5) . This figure demonstrates that although the errors are larger (∼7 m/s) in the regions of no or scant data, the model is reasonably constrained in such regions.

5.3 Kp Dependence

Figures 9 and 10 show the Kp dependence of northern and southern high-latitude thermospheric winds, respectively. The figures show wind components as a function of Kp for various 5-degree MLAT bins. The results are presented at 4 equally spaced 3-hour MLT bins. We have binned and averaged all the space and ground-based data (except GOCE - discussed later in detail in section 5.5) together to calculate the average data points. Data do not exist at all space-time locations, so we calculated HL-TWiM winds only at the space-time locations of data (except GOCE). Both the model and data are binned and averaged in the same way. The winds shown are averaged over all the longitudes and seasons.

As shown in Figures 9 and 10, HL-TWiM captures the overall morphology of Kp variation of high-latitude winds. HL-TWiM and observational data agree well at low and moderate Kp, whereas discrepancies exist at high Kp (>6). In both the NH and SH, model meridional winds agree better with data than zonal winds (also discussed in section 5.2). Also, the overall agreement between model and data is better in SH than NH. The largest discrepancies between model and data zonal winds, up to 200 m/s, exist at northern latitudes between 75 and 80 MLAT in 6-9 MLT and 12-15 MLT bins (Figure 9). Other than WINDII, GOCE is the biggest contributor of data between 75 and 80 MLAT in 6-9 MLT and could be driving these discrepancies.

The discontinuities (sharp jumps) in winds, for example in zonal winds in Figure 10 in 0600-0900 MLT and 80-85S MLAT bin between Kp 5 and 8, are due to the averaging over all seasons and longitudes. In this bin, some longitudes or seasons may be contributing more than the other longitudes and seasons in the neighboring bins. As discussed in the model formulation section, the Kp spline functions used to present Kp dependence of winds in HL-TWiM are tapered at lower and higher end Kp values. The model and data winds agree at low end Kp values; it shows that tapering at lower Kp works well. However, tapering at high end Kp is required because the data required for robust wind modeling for high Kp (>6) is not yet available.

Polar plots showing modeled Kp dependence in the wind field are shown in the bottom row in Figures 9 and 10. They expose the strong control of geomagnetic activity on strength, shape, latitudinal extent of large-scale wind circulation.

5.4 UT and Longitude Dependence

The high-latitude ionospheric convection (which is the primary driver of high-latitude wind circulation) shows UT dependence (e.g., Bekerat et al., 2003; Ruohoniemi & Greenwald, 2005). It primarily arises due to the offset between geographic and geomagnetic poles (and hence different solar illumination and ionospheric conductivity) (e.g., Ruohoniemi & Greenwald, 2005). The high-latitude wind patterns are also expected to show UT dependence (Killeen et al., 1983; Roble et al., 1984; Rees & Fuller-Rowell, 1989; Fuller-Rowell et al., 1988), but the UT dependence of high-latitude neutral circulation has been rarely studied. Here we studied UT dependence via the MLON and MLT arguments.

First, we calculated an equal area geographic grid (geographic latitude and longitude - icosahedron grid (Teanby, 2006)) for full year (at 30-day interval) at every UT for Kp=3. The use of an icosahedron grid (equal area) allowed us to generate a regular latitude-longitude grid without overpopulating the model output closer to the geographic poles where all the longitudes converge. When the icosahedron geographic grid is projected onto geomagnetic coordinates, it creates a similar grid in geomagnetic coordinates. Then we calculated the corresponding MLAT, MLON, and MLT using geographic latitude, geographic longitude, and UT and supplied the calculated MLAT, MLON, and MLT as input to HL-TWiM. The equal area icosahedron grid in geomagnetic coordinates is shown in the supporting information Figure S6.

The UT dependences of high-latitude model winds for NH and SH are shown in Figure 11. The winds are binned and averaged as a function of MLAT and MLT for five 60-day bins, except the bin (DOY 120-240). The seasonal bin DOY 120-240 represents full summer for NH and winter for SH. The winds are further binned into two different UTs (0-4 UT and 12-16 UT). For an easy interpretation of the UT dependence of winds, a difference plot between 0-4 UT and 12-16 UT winds is shown in supporting information Figure S7.

The overall wind patterns look similar at both UTs, but there are many subtle differences that can be seen in almost all the panels. For example, in Figure 11, the SH winter DOY bin 120-240 zonal winds for 0-4 UT between 0000 and 0200 MLT are mostly westward, but for 12-16 UT, they are strongly eastward with a difference of ∼175 m/s. Similarly, NH zonal winds above 80 MLAT around 0700 MLT for 12-16 UT are >75 m/s more westward than 00-04 UT. Overall, UT changes are stronger in SH than NH as illustrated in Figure S7. The differences in different seasons (as in Figure S7) appear similar because in HL-TWiM, MLON and DOY are uncoupled.

We also looked at the UT dependence of winds from a different perspective by plotting polar vector winds (shown in Figure 12). Because UT and seasons are not coupled in the model, here winds are averaged over all the seasons. Figure 12 illustrates the changes in high-latitude neutral circulation with UT (and Kp) and their inter-hemispheric differences. In both the hemispheres, the most significant changes in winds with UT are present on the nightside. The UT dependence of winds is much more visible at low Kp in both the hemispheres.

5.5 Seasonal Dependence and GOCE Analyses

This study observationally shows the seasonal variation in high-latitude thermospheric winds in unprecedented detail, with the help of GOCE and WINDII's extensive seasonal wind coverage. The GOCE orbit is almost fixed in local time, thus it prevents any cross-contamination between local time and seasonal variations. Even though the GOCE data are limited to a narrow band around the dawn and dusk periods, it is the only F region thermospheric wind database that provides full seasonal coverage. GOCE MLAT coverage in a particular MLT band is narrow in the NH, but it is much wider in the south because of larger offset of the south geomagnetic pole from the Earth's rotation axis than the north geomagnetic pole. A major portion of the GOCE lifespan was in solar minimum conditions and only a small number of high geomagnetic activity events cropped up during that time period. Compared to GOCE, WINDII's DOY coverage is sporadic when divided into multiple bins.

As discussed in sections 2 and 3, GOCE data are in the form of cross-track winds, which is the component of actual wind normal to the satellite path (from left to right relative to the satellite motion). Thus, the measured single component of the GOCE cross-track wind cannot be projected into any geographically meaningful coordinate frame (geographic or geomagnetic). Therefore, for a direct comparison between GOCE, HL-TWiM, and other stations, we projected HL-TWiM and other observational wind databases along the GOCE cross-track winds.

Because of the larger number of possible data bins as function of MLAT, MLON, DOY, and Kp, it is not possible to include all the cross-track comparisons in the main text; however, we have selected two figures for main text (one for NH and other for SH) when GOCE data presence is significant in most of the bins (Figures 13 and 14). The rest of the comparisons between the cross-track winds from GOCE, HL-TWiM, and other stations as a function of DOY for various Kp and MLAT bins (5 degree) are included in the supporting information (Figures S8 to S29). HL-TWiM winds are evaluated at the locations of GOCE, and then projected along the GOCE cross-track wind directions. MLT bins are kept narrow (1-hour bins) since winds near dusk and dawn can change drastically with MLT and hence bigger MLT bins can create unrealistic jumps in winds. When GOCE data are absent, no cross-track winds from other datasets can be generated. The rightmost column in each of these figures titled 'GOCE unit vectors' illustrate the average direction of cross-track winds in geomagnetic coordinates; x-axis is the zonal and y-axis is meridional direction. For reference, vector orientation towards the top of the page represents geomagnetic north. In the SH, due to the wide geographic coverage of GOCE in MLAT-MLT, GOCE cross-track directions vary widely at polar latitudes, causing distorted behavior of some of the average unit vectors. This is presumably also causing GOCE and other dataset discrepancies in polar MLAT bins where the cross-track directions vary widely. But north of 70S MLAT, GOCE cross-track directions in each bin are aligned.

There are many differences in the GOCE and other station cross-track winds. Nevertheless, all of them show similar seasonal variation in winds. The agreement between GOCE and the model is generally good at middle latitudes and auroral latitudes and discrepancies increase with increasing latitude. The discrepancies between other data and GOCE drive the model fits away from GOCE winds; this occurs mostly in the SH.

The seasonal (DOY) and Kp variations in winds are evident in this analysis. Winds show strong seasonality and Kp dependence in both NH and SH. The signal of annual variation in winds is evident in all of them. The seasonal variation in winds changes with latitude. Overall the middle latitude winds (both in NH and SH) respond the least to the changes in seasons compared to the upper latitudes.

Interestingly, as evident in many of the Figures between S8 and S29 (including Figures 13 and 14), in addition to the annual oscillation (AO), GOCE suggests a semi-annual oscillation (SAO) like modulation of horizontal thermospheric winds; it is clearly visible in data for |MLAT| <70 (e.g., Figures 13 and 14) and is present in both the hemispheres. Such variations are also present in the GOCE vertical wind activity as discussed in Visser et al. (2019). Emmert et al. (2003) showed the presence of SAO in meridional winds at Millstone Hill under solar minimum conditions. A major part of the GOCE life span was under solar minimum conditions. SAO modulation in winds is not clear in other databases; it could be because either they do not have enough DOY coverage or we have averaged their data over a wide range of $F10.7$ values.

The SAO is a dominant mode of seasonal variability in the global stratosphere and mesosphere, and has been studied extensively in the lower thermosphere. The SAO variation in thermospheric density is well known as well (e.g., Emmert, 2015). An SAO in thermospheric winds on a large scale has never been observed before, in part, perhaps, because the full seasonal variation of ground-based or space-based observations has never been studied before (WINDII's DOY coverage is sporadic when divided into multiple bins). In any case, further focused studies are required to extract such behavior from wind measurements and investigate their origin.

6 Summary and Future Steps

Large-scale studies of high-latitude winds are rare. Southern high-latitude wind studies are even more rare and the majority of them refer to summer sunlit conditions. Past high-latitude studies have been primarily focused on the northern high latitudes. In Dhadly et al. (2017, 2018), we studied northern high-latitude winds as a function of MLAT and MLT using broad seasonal and Kp bins. The full DOY, MLON, and UT variations of high-latitude wind are still poorly understood. The results presented here are the most comprehensive to date of large-scale NH and SH high-latitude thermospheric wind circulation as a function of DOY, MLAT, MLON, MLT, and Kp.

In this study, we developed an F region empirical model of high-latitude thermosphere winds (HL-TWiM) in Quasi-Dipole geomagnetic coordinates based on extensive statistical analyses of long-term thermospheric neutral wind observations from 21 ground-based (FPIs and SDIs) and 2 space-based instruments (UARS WINDII and GOCE). HL-TWiM provides a comprehensive specification of high-latitude F region horizontal neutral winds as a function of DOY, MLAT, MLON, MLT, and Kp in geomagnetic coordinates. Leveraging the ideas from earlier wind studies, the MLAT and MLT dependences in HL-TWiM are constructed using vector spherical harmonics, DOY and MLON variations are constructed using simple harmonic functions, and Kp dependence is constructed using quadratic B-splines.

Extensive comparisons between data and HL-TWiM at northern and southern high latitudes show that overall the HL-TWiM captures most of the climatological variations evident in the data. Statistical metrics shown in Table 2 demonstrate a significant improvement in HL-TWiM winds over HWM14. This multi-instrument study sets a necessary benchmark for validating new high-latitude observations and tuning first-principles models. One such operation was executed in this study: correcting GOCE cross-track wind bias. We statistically quantified the apparent GOCE cross-track bias as a function of MLAT and applied it as a correction profile to the GOCE measurements. This reduced the bias in SH GOCE cross-track winds from 92 m/s to 38 m/s and root mean square difference from 112 m/s to 49 m/s compared to WINDII.

This study shows stronger UT changes in thermospheric horizontal winds in SH than NH. In both the hemispheres, the most significant changes in winds with UT occur on the nightside. Also, the UT dependence is much more visible under quiet geomagnetic conditions. Neutral winds show strong annual variation as evident in data and HL-TWiM output. GOCE data suggests the presence of SAO like modulation of horizontal winds and this variation is present in both the hemispheres; however, SAO modulation in winds is not clear in other databases. Further focused studies are required to extract such behavior from winds and study their origins.

Many studies have show the importance of $F10.7$ and the orientation of the interplanetary magnetic field (IMF) on wind circulation, but it is notoriously difficult to parametrize their associated wind behaviors yet as the sample sizes become too small after binning data into desired bins for any definitive large-scale climatological conclusions to be drawn. Formulating $F10.7$ and IMF dependences in HL-TWiM would be a significant enhancement for space weather applications. As new data from high latitudes accumulate, it may be possible in the near future to parametrize their wind behaviors without averaging over many other important factors. In the future, we plan to upgrade the HWM14 by replacing the DWM07 with HL-TWiM at high latitudes; DWM07 calculates global perturbation winds as functions of MLAT, MLT, and Kp, but does not consider seasonal and longitudinal variation of winds. Updating HWM14 with HL-TWiM would significantly improve its high-latitude functionally.

Acknowledgments

This study was supported by NASA's Heliophysics Supporting Research Program (grant NNH16AC38I). Poker Flat and Toolik Lake SDI data are available at http://sdi server.gi.alaska.edu/sdiweb/index.asp. UARS WINDII data are available at http://www.asc-csa.gc.ca/eng/open-data/access-the-data.asp. GOCE data can be obtained from https://earth.esa.int/web/guest/miss operational-missions/goce/air-density-and-crosswind-data. Longyearbyen, Kiruna, and Sodankyla FPI data are available at DOI: 10.5522/04/9741977, DOI: 10.5522/04/9742070, and DOI: 10.5522/04/9742133. HIWIND can be obtained from https://doi.org/10.5065/ad71-8827. Kp and $F10.7$ indexes are available at NASA OMNIWeb data explorer (http://omniweb.gsfc.nasa.gov/form/dx All other data sets can be obtained from the Madrigal database at http://cedar.openmadrigal.org/cgi-bin/accessData.cgi. Poker Flat and Toolik Lake SDI operations (during the observing periods included in this manuscript) were supported by the National Science Foundation through grant numbers AGS1243476, AGS1140075, and AGS0821431. Resolute Bay FPI was supported by the National Science Foundation through grant AGS1339918. For Peach Mountain and Urbana FPIs, work at the University of Illinois was supported by the National Science Foundation through grants AGS 1452291 and ATM1452097. For the Longyearbyen, Kiruna and Sodankyla FPIs, work at University College London was supported by NERC grants NE/P001556/1 and NE/N004051/1, and EOARD Grant number FA9550-17-1-0019. The Jang Bogo FPI operation is supported by grant PE19020 from Korea Polar Research Institute (KOPRI). HIWIND operation were supported by NASA grant NNX15AK75G. HL-TWiM software written in FORTRAN-90 is available in the supporting information.

References

Aruliah, A. L., Farmer, A. D., Rees, D., & Brändström, U. (1996). The seasonal behavior of high-latitude thermospheric winds and ion velocities observed over one solar cycle. *J. Geophys. Res.*, *101*(A7), 15701. Retrieved from `http://doi.wiley.com/10.1029/96JA00360` doi: 10.1029/96JA00360

Aruliah, A. L., & Griffin, E. (2001). Evidence of meso-scale structure in the high-latitude thermosphere. *Ann. Geophys.*, *19*(1), 37–46. Retrieved from `http://www.ann-geophys.net/19/37/2001/` doi: 10.5194/angeo-19-37-2001

Aruliah, A. L., Griffin, E. M., Aylward, A. D., Ford, E. A. K., Kosch, M. J., Davis, C. J., ... Jussila, J. (2005, jan). First direct evidence of meso-scale variability on ion-neutral dynamics using co-located tristatic FPIs and EISCAT radar in Northern Scandinavia. *Ann. Geophys.*, *23*(1), 147–162. Retrieved from `http://www.ann-geophys.net/23/147/2005/` doi: 10.5194/angeo-23-147-2005

Aruliah, A. L., Griffin, E. M., McWhirter, I., Aylward, A. D., Ford, E. A. K., Charalambous, A., ... Howells, V. S. C. (2004). First tristatic studies of meso-scale ion-neutral dynamics and energetics in the high-latitude upper atmosphere using collocated FPIs and EISCAT radar. *Geophys. Res. Lett.*, *31*(3), L03802. Retrieved from `http://dx.doi.org/10.1029/2003GL018469` doi: 10.1029/2003gl018469

Aruliah, A. L., Rees, D., & Fuller-Rowell, T. J. (1991). The combined effect of solar and geomagnetic activity on high latitude thermospheric neutral winds. Part I. Observations. *J. Atmos. Terr. Phys.*, *53*(6-7), 467–483. Retrieved from `http://www.sciencedirect.com/science/article/pii/002191699190075I` doi: http://dx.doi.org/10.1016/0021-9169(91)90075-I

Bekerat, H. A., Schunk, R. W., & Scherliess, L. (2003). Evaluation of statistical convection patterns for real-time ionospheric specifications and forecasts. *J. Geophys. Res.*, *108*(A12), 1413. Retrieved from `http://doi.wiley.com/10.1029/2003JA009945` doi: 10.1029/2003JA009945

Chisham, G., Lester, M., Milan, S. E., Freeman, M. P., Bristow, W. A., Grocott, A., ... Walker, A. D. M. (2007, jun). A decade of the Super Dual Auroral Radar Network (SuperDARN): scientific achievements, new techniques and future directions. *Surv. Geophys.*, *28*(1), 33–109. Retrieved from `http://link.springer.com/10.1007/s10712-007-9017-8` doi: 10.1007/s10712-007-9017-8

Conde, M., & Dyson, P. (1995, may). Thermospheric vertical winds above Mawson, Antarctica. *J. Atmos. Terr. Phys.*, *57*(6), 589–596. Retrieved from `http://www.sciencedirect.com/science/article/pii/002191699400099A` doi: 10.1016/0021-9169(94)00099-A

Conde, M., & Smith, R. W. (1995). Mapping thermospheric winds in the auroral zone. *Geophys. Res. Lett.*, *22*(22), 3019–3022. doi: 10.1029/95GL02437

Crickmore, R. I. (1994). Mean thermospheric winds observed from Halley, Antarctica. *Ann. Geophys.*, *12*(10/11), 1101–1113. Retrieved from `http://www.ann-geophys.net/12/1101/1994/` doi: 10.1007/s00585-994-1101-5

Crowley, G., Emery, B. A., Roble, R. G., Carlson, H. C., & Knipp, D. J. (1989). Thermospheric dynamics during September 18-19, 1984: 1. Model simulations. *J. Geophys. Res.*, *94*(A12), 16925. Retrieved from `http://doi.wiley.com/10.1029/JA094iA12p16925` doi: 10.1029/JA094iA12p16925

Crowley, G., Emery, B. A., Roble, R. G., Carlson, H. C., Salah, J. E., Wickwar, V. B., ... Marcos, F. A. (1989). Thermospheric dynamics during September 18-19, 1984: 2. Validation of the NCAR Thermospheric General Circulation Model. *J. Geophys. Res.*, *94*(A12), 16945. Retrieved from `http://doi.wiley.com/10.1029/JA094iA12p16945` doi: 10.1029/JA094iA12p16945

Dhadly, M., & Conde, M. (2017, jun). Trajectories of thermospheric air parcels flowing over Alaska, reconstructed from ground-based wind measurements. *J. Geophys. Res. Sp. Phys.*, *122*(6), 6635–6651. Retrieved from `http://doi.wiley.com/10.1002/2017JA024095` doi: 10.1002/2017JA024095

Dhadly, M., Emmert, J., Drob, D., Conde, M., Doornbos, E., Shepherd, G., ... Ridley, A. (2017). Seasonal dependence of northern high-latitude upper thermospheric winds: A quiet time climatological study based on ground-based and space-based measurements. *J. Geophys. Res. Sp. Phys.*, *122*(2), 2619–2644. Retrieved from `http://doi.wiley.com/10.1002/2016JA023688` doi: 10.1002/2016JA023688

Dhadly, M., Emmert, J. T., Drob, D. P., Conde, M. G., Doornbos, E., Shepherd, G., ... Ridley, A. (2018, jan). Seasonal Dependence of Geomagnetic Active-Time Northern High-Latitude Upper Thermospheric Winds. *J. Geophys. Res. Sp.*

Phys., *123*(1), 739–754. Retrieved from http://doi.wiley.com/10.1002/2017JA024715 doi: 10.1002/2017JA024715

Dhadly, M., Meriwether, J., Conde, M., & Hampton, D. (2015, nov). First ever cross comparison of thermospheric wind measured by narrow- and wide-field optical Doppler spectroscopy. *J. Geophys. Res. Sp. Phys.*, *120*(11), 9683–9705. Retrieved from http://doi.wiley.com/10.1002/2015JA021316 doi: 10.1002/2015JA021316

Doornbos, E. (2011). *Thermospheric Density and Wind Determination from Satellite Dynamics.* Delft, Netherlands. doi: 10.1007/978-3-642-25129-0

Doornbos, E., Bruinsma, S., Fritsche, B., Visser, P., Van Den IJssel, J., Encarnacao, J. T., & Kern, M. (2013). Air Density And Wind Retrieval Using GOCE Data. *ESA Living Planet Symp. Proc. Conf. held 9-13 Sept. 2013 Edinburgh United Kingdom. ESA SP-722. 2-13, p.7*, *722*, 7.

Doornbos, E., Bruinsma, S. L., Fritsche, B., Koppenwallner, G., Visser, P., Van Den IJssel, J., & Teixeira da Encarnação, J. (2014). GOCE+ Theme 3: Air density and wind retrieval using GOCE data final report. *Tech. Rep.*, *Tech. Rep.*(4000102847/NL/EL, TU Delft, Netherlands).

Doornbos, E., Den IJssel, J. V., Lühr, H., Förster, M., Koppenwallner, G., Bruinsma, S., … Perosanz, F. (2010, jul). Neutral Density and Crosswind Determination from Arbitrarily Oriented Multiaxis Accelerometers on Satellites. *J. Spacecr. Rockets*, *47*(4), 580–589. Retrieved from http://arc.aiaa.org/doi/abs/10.2514/1.48114 doi: 10.2514/1.48114

Drob, D. P., Emmert, J. T., Meriwether, J. W., Makela, J. J., Doornbos, E., Conde, M., … Klenzing, J. H. (2015, apr). An update to the Horizontal Wind Model (HWM): The quiet time thermosphere. *Earth Sp. Sci.*, *2*. Retrieved from http://doi.wiley.com/10.1002/2014EA000089 doi: 10.1002/2014EA000089

Emmert, J. T. (2015, apr). Altitude and solar activity dependence of 1967-2005 thermospheric density trends derived from orbital drag. *J. Geophys. Res. Sp. Phys.*, *120*(4), 2940–2950. Retrieved from http://doi.wiley.com/10.1002/2015JA021047 doi: 10.1002/2015JA021047

Emmert, J. T., Drob, D. P., Shepherd, G. G., Hernandez, G., Jarvis, M. J., Meriwether, J. W., … Tepley, C. A. (2008, nov). DWM07 global empirical model of upper thermospheric storm-induced disturbance winds. *J. Geophys. Res.*, *113*(A11), A11319. Retrieved from http://doi.wiley.com/10.1029/2008JA013541 doi: 10.1029/2008JA013541

Emmert, J. T., Faivre, M. L., Hernandez, G., Jarvis, M. J., Meriwether, J. W., Niciejewski, R. J., … Tepley, C. A. (2006, dec). Climatologies of nighttime upper thermospheric winds measured by ground-based Fabry-Perot interferometers during geomagnetically quiet conditions: 1. Local time, latitudinal, seasonal, and solar cycle dependence. *J. Geophys. Res.*, *111*(A12), A12302. Retrieved from http://doi.wiley.com/10.1029/2006JA011948 doi: 10.1029/2006JA011948

Emmert, J. T., Fejer, B. G., Shepherd, G. G., & Solheim, B. H. (2002, dec). Altitude dependence of middle and low-latitude daytime thermospheric disturbance winds measured by WINDII. *J. Geophys. Res. Sp. Phys.*, *107*(A12), SIA 19–1–SIA 19–15. Retrieved from http://doi.wiley.com/10.1029/2002JA009646 doi: 10.1029/2002JA009646

Emmert, J. T., Fejer, B. G., & Sipler, D. P. (2003). Climatology and latitudinal gradients of quiet time thermospheric neutral winds over Millstone Hill from Fabry-Perot interferometer measurements. *J. Geophys. Res.*, *108*(A5), 1196. Retrieved from http://doi.wiley.com/10.1029/2002JA009765 doi: 10.1029/2002JA009765

Emmert, J. T., Hernandez, G., Jarvis, M. J., Niciejewski, R. J., Sipler, D. P., & Vennerstrom, S. (2006, dec). Climatologies of nighttime upper thermospheric winds measured by ground-based Fabry-Perot interferometers during geomagnetically quiet conditions: 2. High-latitude circulation and interplanetary magnetic field dependence. *J. Geophys. Res.*, *111*(A12), A12303. Retrieved from http://doi.wiley.com/10.1029/2006JA011949 doi: 10.1029/2006JA011949

Emmert, J. T., Richmond, a. D., & Drob, D. P. (2010, aug). A computationally compact representation of Magnetic-Apex and Quasi-Dipole coordinates with smooth base vectors. *J. Geophys. Res.*, *115*(A8), A08322. Retrieved from http://doi.wiley.com/10.1029/2010JA015326 doi: 10.1029/2010JA015326

Förster, M., & Cnossen, I. (2013, sep). Upper atmosphere differences between northern and southern high latitudes: The role of magnetic field asymmetry. *J. Geophys. Res. Sp. Phys.*, *118*(9), 5951–5966. Retrieved from http://doi.wiley.com/10.1002/jgra.50554 doi: 10.1002/jgra.50554

Förster, M., Haaland, S. E., & Doornbos, E. (2011, jan). Thermospheric vorticity at high geomagnetic latitudes from CHAMP data and its IMF dependence. *Ann. Geophys.*, *29*(1), 181–186. Retrieved from http://www.ann-geophys.net/29/181/2011/angeo-29-181-2011.html doi: 10.5194/angeo-29-181-2011

Fuller-Rowell, T. J., Rees, D., Quegan, S., Moffett, R. J., & Bailey, G. J. (1988). Simulations of the seasonal and universal time variations of the high-latitude thermosphere and ionosphere using a coupled, three-dimensional, model. *Pure Appl. Geophys. PAGEOPH*, *127*(2-3), 189–217. Retrieved from http://link.springer.com/10.1007/BF00879811 doi: 10.1007/BF00879811

Griffin, E. M., Aruliah, A., Müller-Wodarg, I. C. F., & Aylward, A. (2004, mar). Comparison of high-latitude thermospheric meridionalwinds II: combined FPI, radar and model Climatologies. *Ann. Geophys.*, *22*(3), 863–876. Retrieved from http://www.ann-geophys.net/22/863/2004/angeo-22-863-2004.html doi: 10.5194/angeo-22-863-2004

Griffin, E. M., Aruliah, A. L., McWhirter, I., & Yeoman, T. (2002). Thermospheric neutral temperature measurements from the University College London Fabry-Perot interferometers. *Sadankyla Geophys. Obs. Publ.*, *92*, 117–120. Retrieved from http://www.researchgate.net/publication/237620996{_}Thermospheric{_}Neutral{_}Temperature{_}Measurements{_}from{_}the{_}University{_}College{_}London{_}Fabry-Perot{_}Interferometers

Hays, P. B., Killeen, T. L., Spencer, N. W., Wharton, L. E., Roble, R. G., Emery, B. A., . . . Craven, J. D. (1984). Observations of the dynamics of the polar thermosphere. *J. Geophys. Res. Sp. Phys.*, *89*(A7), 5597–5612. Retrieved from http://dx.doi.org/10.1029/JA089iA07p05597 doi: 10.1029/JA089iA07p05597

Hernandez, G., McCormac, F. G., & Smith, R. W. (1991). Austral thermospheric wind circulation and interplanetary magnetic field orientation. *J. Geophys. Res.*, *96*(A4), 5777. Retrieved from http://doi.wiley.com/10.1029/90JA02458 doi: 10.1029/90JA02458

Hernandez, G., & Roble, R. G. (1995). Thermospheric nighttime neutral temperature and winds over Fritz Peak Observatory: Observed and calculated solar cycle variation. *J. Geophys. Res.*, *100*(A8), 14647. Retrieved from http://doi.wiley.com/10.1029/95JA00565 doi: 10.1029/95JA00565

Hernandez, G., & Roble, R. G. (2003, may). Simultaneous thermospheric observations during the geomagnetic storm of April 2002 from South Pole and Arrival Heights, Antarctica. *Geophys. Res. Lett.*, *30*(10), n/a–n/a. Retrieved from http://doi.wiley.com/10.1029/2003GL016878 doi: 10.1029/2003GL016878

Killeen, T. L., Hays, P. B., Spencer, N. W., & Wharton, L. E. (1982). Neutral winds in the polar thermosphere as measured from Dynamics Explorer. *Geo-*

phys. Res. Lett., *9*(9), 957–960. doi: 10.1029/GL009i009p00957

Killeen, T. L., Hays, P. B., Spencer, N. W., & Wharton, L. E. (1983). NEUTRAL WINDS IN THE POLAR THERMOSPHERE AS MEASURED FROM DYNAMICS EXPLORER. *Adv. Sp. Res*, *2*(10), 133–169. Retrieved from `https://deepblue.lib.umich.edu/bitstream/handle/2027.42/24099/0000356.pdf;sequence=1` doi: 0273-1177/83/100133-04$03.00/O

Killeen, T. L., Won, Y.-I., Niciejewski, R. J., & Burns, A. G. (1995). Upper thermosphere winds and temperatures in the geomagnetic polar cap: Solar cycle, geomagnetic activity, and interplanetary magnetic field dependencies. *J. Geophys. Res.*, *100*(A11), 21327. Retrieved from `http://doi.wiley.com/10.1029/95JA01208` doi: 10.1029/95JA01208

Lee, C., Jee, G., Wu, Q., Shim, J. S., Murphy, D., Song, I.-S., ... Kim, Y. H. (2017, sep). Polar Thermospheric Winds and Temperature Observed by Fabry-Perot Interferometer at Jang Bogo Station, Antarctica. *J. Geophys. Res. Sp. Phys.*, *122*(9), 9685–9695. Retrieved from `http://doi.wiley.com/10.1002/2017JA024408` doi: 10.1002/2017JA024408

Makela, J. J., Meriwether, J. W., Huang, Y., & Sherwood, P. J. (2011). Simulation and analysis of a multi-order imaging Fabry-Perot interferometer for the study of thermospheric winds and temperatures. *Appl. Opt.*, *50*(22), 4403–4416. Retrieved from `http://ao.osa.org/abstract.cfm?URI=ao-50-22-4403` doi: 10.1364/ao.50.004403

Meriwether, J. W. (2006). Studies of thermospheric dynamics with a Fabry-Perot interferometer network: A review. *J. Atmos. Sol. Terr. Phys.*, *68*(13), 1576–1589. Retrieved from `http://www.sciencedirect.com/science/article/pii/S1364682606001192` doi: 10.1016/j.jastp.2005.11.014

Meriwether, J. W., Killeen, T. L., McCormac, F. G., Burns, A. G., & Roble, R. G. (1988). Thermospheric winds in the geomagnetic polar cap for solar minimum conditions. *J. Geophys. Res.*, *93*(A7), 7478. Retrieved from `http://doi.wiley.com/10.1029/JA093iA07p07478` doi: 10.1029/JA093iA07p07478

Pallamraju, D. (2005). First ground-based measurements of OI 6300 Å daytime aurora over Boston in response to the 30 October 2003 geomagnetic storm. *Geophys. Res. Lett.*, *32*(3), L03S10. Retrieved from `http://doi.wiley.com/10.1029/2004GL021417` doi: 10.1029/2004GL021417

Picone, J. M., Hedin, A. E., Drob, D. P., & Aikin, A. C. (2002). NRLMSISE-00 empirical model of the atmosphere: Statistical comparisons and scientific issues. *J. Geophys. Res.*, *107*(A12), 1468. Retrieved from `http://doi.wiley.com/10.1029/2002JA009430` doi: 10.1029/2002JA009430

Rees, D., & Fuller-Rowell, T. J. (1989). The response of the thermosphere and ionosphere to magnetospheric forcing. *Philos. Trans. R. Soc. London. Ser. A, Math. Phys. Sci.*, *328*(18), 139–171. Retrieved from `http://www.jstor.org/stable/38229http://about.jstor.org/terms:04http://about.jstor.org/terms`

Rees, D., Fuller-Rowell, T. J., Gordon, R., Killeen, T. L., Hays, P. B., Wharton, L., & Spencer, W. (1983). A comparison of wind observations of the upper thermosphere from the Dynamics Explorer satellite with the predictions of a global time-dependent model. *Planet. Sp. Sci.*, *31*(11), 1299–1314. doi: 10.1016/0032-0633(83)90067-3

Richmond, A. D. (1995). Ionospheric electrodynamics using magnetic apex coordinates. *J. Geomagn. Geoelectr.*, *47*(2), 191–212. doi: 10.5636/jgg.47.191

Richmond, A. D., Lathuillere, C., & Vennerstroem, S. (2003). Winds in the high-latitude lower thermosphere: Dependence on the interplanetary magnetic field. *J. Geophys. Res.*, *108*(A2), 1066. Retrieved from `http://doi.wiley.com/10.1029/2002JA009493` doi: 10.1029/2002JA009493

Roble, R. G., Emery, B. A., Dickinson, R. E., Ridley, E. C., Killeen, T. L., Hays, P. B., ... Spencer, N. W. (1984). Thermospheric circulation, temperature, and compositional structure of the southern hemisphere polar cap during October?November 1981. *J. Geophys. Res.*, *89*(A10), 9057. Retrieved from http://doi.wiley.com/10.1029/JA089iA10p09057 doi: 10.1029/JA089iA10p09057

Ruohoniemi, J. M., & Greenwald, R. A. (2005, sep). Dependencies of high-latitude plasma convection: Consideration of interplanetary magnetic field, seasonal, and universal time factors in statistical patterns. *J. Geophys. Res. Sp. Phys.*, *110*(A9). Retrieved from http://doi.wiley.com/10.1029/2004JA010815 doi: 10.1029/2004JA010815

Shepherd, G., & Shepherd, M. (2018, may). High-Latitude Observations of a Localized Wind Wall and Its Coupling to the Lower Thermosphere. *Geophys. Res. Lett.*, *45*(10), 4586–4593. Retrieved from http://doi.wiley.com/10.1029/2018GL077722 doi: 10.1029/2018GL077722

Shepherd, G., Thuillier, G., Cho, Y.-M., Duboin, M.-L., Evans, W. F. J., Gault, W. A., ... Ward, W. E. (2012, jun). The Wind Imaging Interferometer (WINDII) on the Upper Atmosphere Research Satellite: A 20 year perspective. *Rev. Geophys.*, *50*(2). Retrieved from http://doi.wiley.com/10.1029/2012RG000390 doi: 10.1029/2012RG000390

Shepherd, M., Shepherd, G., & Codrescu, M. (2019, jun). Perturbations of O(1 D) VER, temperature, winds, atomic oxygen and TEC at high southern latitudes. *J. Geophys. Res. Sp. Phys.*, 2019JA026480. Retrieved from https://onlinelibrary.wiley.com/doi/abs/10.1029/2019JA026480 doi: 10.1029/2019JA026480

Sipler, D. P., Hagan, M. E., Zipf, M. E., & Biondi, M. A. (1991). Combined optical and radar wind measurements in the F region over Millstone Hill. *J. Geophys. Res.*, *96*(A12), 21255. Retrieved from http://doi.wiley.com/10.1029/91JA02371 doi: 10.1029/91JA02371

Smith, R., & Hernandez, G. (1995, may). Vertical winds in the thermosphere within the polar cap. *J. Atmos. Terr. Phys.*, *57*(6), 611–620. Retrieved from http://www.sciencedirect.com/science/article/pii/002191699400101S doi: 10.1016/0021-9169(94)00101-S

Smith, R. W., Hernandez, G., Price, K., Fraser, G., Clark, K. C., Schulz, W. J., ... Clark, M. (1994, sep). The June 1991 thermospheric storm observed in the southern hemisphere. *J. Geophys. Res.*, *99*(A9), 17609. Retrieved from http://doi.wiley.com/10.1029/94JA01101 doi: 10.1029/94JA01101

Smith, R. W., Rees, D., & Stewart, R. D. (1988). Southern hemisphere thermospheric dynamics: A review. *Rev. Geophys.*, *26*(3), 591. Retrieved from http://doi.wiley.com/10.1029/RG026i003p00591 doi: 10.1029/RG026i003p00591

Strickland, D. J., Cox, R. J., Meier, R. R., & Drob, D. P. (1999). Global O/N2 derived from DE 1 FUV dayglow data: Technique and examples from two storm periods. *J. Geophys. Res.*, *104*(A3), 4251. Retrieved from http://doi.wiley.com/10.1029/98JA02817 doi: 10.1029/98JA02817

Teanby, N. (2006, nov). An icosahedron-based method for even binning of globally distributed remote sensing data. *Comput. Geosci.*, *32*(9), 1442–1450. Retrieved from https://www.sciencedirect.com/science/article/pii/S0098300406000173{\#}sec6 doi: 10.1016/J.CAGEO.2006.01.007

Visser, T., Doornbos, E. N., de Visser, C. C., Visser, P. N., & Fritsche, B. (2018, sep). Torque model verification for the GOCE satellite. *Adv. Sp. Res.*, *62*(5), 1114–1136. Retrieved from https://www.sciencedirect.com/science/article/pii/S027311771830509X?via{\%}3Dihub doi: 10.1016/J.ASR.2018.06.025

Visser, T., March, G., Doornbos, E., de Visser, C., & Visser, P. (2019, jan). Horizontal and vertical thermospheric cross-wind from GOCE linear and angular accelerations. *Adv. Sp. Res.*. Retrieved from https://www.sciencedirect.com/

science/article/pii/S027311771930050X doi: 10.1016/J.ASR.2019.01.030
Wharton, L. E., Spencer, N. W., & Mayr, H. G. (1984, may). The Earth's thermospheric superrotation from Dynamics Explorer 2. *Geophys. Res. Lett.*, *11*(5), 531–533. Retrieved from http://doi.wiley.com/10.1029/GL011i005p00531 doi: 10.1029/GL011i005p00531
Wu, Q., Gablehouse, R. D., Solomon, S. C., Killeen, T. L., & She, C.-Y. (2004, dec). A New Fabry-Perot Interferometer for Upper Atmosphere Research. In C. A. Nardell, P. G. Lucey, J.-H. Yee, & J. B. Garvin (Eds.), *Proc. spie* (Vol. 5660, pp. 218–227). Retrieved from http://adsabs.harvard.edu/abs/2004SPIE.5660..218W doi: 10.1117/12.573084
Wu, Q., Knipp, D., Liu, J., Wang, W., Häggström, I., Jee, G., ... Erickson, P. J. (2019, jul). What Do the New 2018 HIWIND Thermospheric Wind Observations Tell Us About High?Latitude Ion?Neutral Coupling During Daytime? *J. Geophys. Res. Sp. Phys.*, 2019JA026776. Retrieved from https://onlinelibrary.wiley.com/doi/abs/10.1029/2019JA026776 doi: 10.1029/2019JA026776
Wu, Q., Knipp, D., Liu, J., Wang, W., Varney, R., Gillies, R., ... Kwak, Y. (2019, oct). HIWIND Observation of Summer Season Polar Cap Thermospheric Winds. *J. Geophys. Res. Sp. Phys.*, 2019JA027258. Retrieved from https://onlinelibrary.wiley.com/doi/abs/10.1029/2019JA027258 doi: 10.1029/2019JA027258
Wu, Q., McEwen, D., Guo, W., Niciejewski, R., Roble, R., & Won, Y.-I. (2008). Long-term thermospheric neutral wind observations over the northern polar cap. *J. Atmos. Solar-Terrestrial Phys.*, *70*(16), 2014–2030. doi: 10.1016/j.jastp.2008.09.004

Figure 1. Location of F region thermospheric wind observations at northern (top row) and southern (bottom row) high latitudes in geographic (left column) and geomagnetic coordinates (right column).

Figure 2. Data distribution as a function of magnetic latitude and local time, of northern (top three panels) and southern (bottom three panels) high-latitude F region thermospheric winds. The data are divided into three broad seasonal bins: December solstice (November, December, January, and February), equinox (March, April, September, and October), and June solstice (May, June, July, and August).

Figure 3. Calculated bias in GOCE cross-winds as function of magnetic latitude for northern and southern high latitudes. This quantification of the bias was applied to GOCE data as a correction profile to correct the apparent bias in the GOCE winds.

Figure 4. Quadratic B-splines used to represent the Kp dependence of HL-TWiM.

Figure 5. Comparison of observed and modeled northern high-latitude F-region geomagnetic zonal winds as a function of MLT (1-hour bins) for consecutive 60-day bins under quiet (Kp<3) and active (Kp≥3) conditions. On the right hand side, to reduce the clutter, only the central location of DOY bin is shown. The station names and geomagnetic activity conditions are shown on the y-axes. Blue represents data from SDIs and FPIs; green and red represent WINDII daytime and nighttime winds at the station location, respectively; the black curve shows the bin-average model winds at the station location; and the light blue curve (mostly hidden behind the black curve) represents the bin-average model winds after evaluating the model at the locations of the data. Error bars indicate the estimated 1σ uncertainty of the mean. Refer to section 5.2 for details.

Figure 6. Same as for Figure 5, but geomagnetic meridional winds are shown here.

Figure 7. Same as for Figure 5, but shown here are geomagnetic zonal winds from southern high-latitude stations. Because of the proximity in location, the first two panels in the first row show winds from three ground-based stations (AH FPI - blue, JB FPI - magenta, MM SDI - orange). Similarly, SP FPI (blue) and SD SDI (magenta) winds are overplotted in the third and fourth panels (first row).

Figure 8. Same as for Figure 7, but for geomagnetic meridional winds from southern high-latitude stations.

Figure 9. Comparison of observed (red) and HL-TWiM (black) geomagnetic zonal (top row) and meridional winds (middle row) from northern high latitudes as a function of Kp for consecutive 5-degree MLAT bins and 4 equally spaced 3-hour MLT bins. HL-TWiM winds are binned after evaluating them at the location of observations. Error bars indicate the estimated 1σ uncertainty of the mean. The bottom row shows HL-TWiM polar wind vectors for Kp 1.5, 3.5, and 5.5 as function of MLAT and MLT. Results are averaged over all seasons. For more details, refer to section 5.3.

Figure 10. Same as for Figure 9, but here for southern high latitudes.

Figure 11. Binned and averaged HL-TWiM zonal and meridional winds for northern (left column) and southern (right column) high latitudes as a function of MLAT and MLT for consecutive 60-day bins. Winds are averaged for 0-4UT and 12-16UT at Kp=3.

Figure 12. Polar wind vector plots for various UTs (0, 8 and 16) and Kp (2 and 5) for northern (top two rows) and southern (bottom two rows) high latitudes as function of MLAT and MLT.

Figure 13. An example of average cross-track wind from northern high latitudes observed by GOCE and computed from FPIs, SDIs, and WINDII as a function of DOY (5-day bin), for successive 5-degree northern MLAT around the dusk and dawn periods and two Kp bins (0-2.5 and 2.5-5). Black symbols show HL-TWiM cross-track wind along the GOCE orbit. All other colors present cross-track winds calculated from different datasets (shown on the top). The rightmost column shows the direction of the average GOCE cross-track unit vector; geomagnetic north (east) is at the top (right) of the page.

Figure 14. Same as Figure 13, but shown here are southern high latitudes.

Table 1. Thermospheric horizontal neutral wind databases used in HL-TWiM. For space-based instruments, data are shown only for |MLAT| > 45.

Station and Short Name	MLAT, MLON	Years of Data	Height (km)	Local Time	References
Northern High-Latitude Datasets					
Fabry-Perot Interferometers (ground-based)					
Thule (TH)	84.6N, 28.9E	1987-1988	250	night	Killeen et al. (1995)
Resolute Bay (RB)	83.6N, 43.5W	2003-2019	250	night	Wu et al. (2004)
Longyearbyen (LY)	74.9N, 113.3E	2010-2013	250	night	Aruliah and Griffin (2001)
Søndre Strømfjord (SS)	73.3N, 41.3E	1983-84,87-95,02-04	250	night	Killeen et al. (1995)
Kiruna (KR)	64.4N, 103.7E	2009-2013	250	night	Aruliah et al. (2005)
Sodankyla (SK)	63.6N, 108.3E	2009-2013	250	night	Aruliah et al. (2005)
Millstone Hill (MH)	53.2N, 5.84E	1990-2002	250	night	Sipler et al. (1991)
Peach Mountain (PM)	53.7N, 12.1W	2012-2015	250	night	Makela et al. (2011)
Urbana (UR)	51.2N, 18.3W	2007-2008, 2012-2015	250	night	Makela et al. (2011)
Scanning Doppler Imaging Fabry-Perot Interferometers (ground-based)					
Toolik Lake (TL)	68.3N, 101.5W	2012-2015	250	night	Conde and Smith (1995)
Poker Flat (PF)	65.2N, 96.7W	2010-2012	250	night	Conde and Smith (1995)
Space-based Instruments					
WINDII 557.7nm	45N-88N	1991-1997	210-320	day	G. Shepherd et al. (2012)
WINDII 630.0nm	45N-86N	1991-1997	210-320	night	G. Shepherd et al. (2012)
GOCE	45N-90N	2009-2013	224-295	twilight	Doornbos et al. (2014)
Southern High-Latitude Datasets					
Fabry-Perot Interferometers (ground-based)					
King Sejong (KS)	47.4S, 11.5E	2017-2018	250	night	Wu et al. (2004)
Palmer (PL)	49.7S, 8.96E	2011-2012	250	night	Wu et al. (2004)
Mount John (MJ)	51.0S, 105.7W	1996	250	night	Hernandez and Roble (1995)
Halley (HA)	62.3S, 28.1E	1988-1998	250	night	Crickmore (1994)
South Pole (SP)	74.1S, 17.6E	1991-1999	250	night	R. Smith and Hernandez (1995)
Jang Bogo (JB)	79.9S, 53.4W	2014-2016	250	night	Lee et al. (2017)
Arrival Heights (AH)	79.9S, 34.2W	2002-2012	250	night	R. Smith and Hernandez (1995)
Scanning Doppler Imaging Fabry-Perot Interferometers (ground-based)					
Mawson (MW)	70.4S, 90.9E	2012-2014	250	night	Conde and Dyson (1995)
South Pole (SD)	74.1S, 17.6E	2016	250	night	Conde and Dyson (1995)
McMurdo (MM)	79.9S, 34.2W	2016-2018	250	night	Conde and Dyson (1995)
Space-based Instruments					
WINDII 557.7nm	45S-88S	1991-1997	210-320	day	G. Shepherd et al. (2012)
WINDII 630.0nm	45S-86S	1991-1997	210-320	night	G. Shepherd et al. (2012)
GOCE	45S-90S	2009-2013	224-295	twilight	Doornbos et al. (2014)

Table 2. Statistical bias (μ_z and μ_m) and root mean square error (σ_z and σ_m) in HL-TWiM wind components (subscript z for zonal and m for meridional wind). HWM14 bias (μ_z^{hwm} and μ_m^{hwm}) and root mean square error (σ_z^{hwm} and σ_m^{hwm}) are shown for reference. Note that, for GOCE, the bias and root mean square error values (shown in italic) are for cross-track winds (not zonal or meridional).

Station	Days	Data Points	μ_z	μ_z^{hwm}	σ_z	σ_z^{hwm}	μ_m	μ_m^{hwm}	σ_m	σ_m^{hwm}
Northern High-Latitude Datasets										
Fabry-Perot Interferometers (ground-based)										
Thule	68	9208	9.93	-12.01	41.43	59.65	1.35	29.36	34.18	68.25
Resolute Bay	1368	67483	25.05	-0.14	34.76	43.91	6.37	10.36	25.86	32.90
Longyearbyen	377	429180	3.08	30.00	24.77	83.51	-6.79	28.06	23.88	73.44
Søndre Strømfjord	892	58344	-19.64	-19.79	52.14	55.72	-14.83	9.78	43.29	43.52
Kiruna	886	548527	-3.83	32.08	17.58	46.82	5.30	31.83	15.58	53.57
Sodankyla	905	351389	6.01	40.81	18.84	50.90	-2.69	18.59	15.00	44.03
Millstone Hill	951	26332	6.57	-0.62	69.34	68.03	1.67	1.99	66.92	68.44
Peach Mountain	594	51074	-0.11	-4.73	23.30	29.78	-13.67	-8.31	30.96	28.91
Urbana	1029	92100	0.82	-3.68	21.24	27.80	-11.97	0.18	26.09	21.16
Scanning Doppler Imaging Fabry-Perot Interferometers (ground-based)										
Toolik Lake	205	292847	-1.95	-6.06	58.54	68.89	6.29	4.17	65.05	66.62
Poker Flat	354	324158	0.07	3.72	59.24	70.56	-8.40	-10.07	62.75	68.01
Space-based Instruments										
WINDII 557.7nm	429	47222	-10.23	-13.34	75.94	79.35	2.50	1.76	64.39	64.66
WINDII 630.0nm	134	7900	11.14	18.75	88.27	89.10	-44.73	-53.93	98.39	107.68
GOCE	1255	110039	*3.85*	*-29.58*	*51.61*	*68.66*	–	–	–	–
Southern High-Latitude Datasets										
Fabry-Perot Interferometers (ground-based)										
King Sejong	333	8098	2.15	33.20	59.23	78.32	-19.06	-69.84	46.52	87.14
Palmer	52	2756	3.65	45.42	55.99	82.18	-0.87	-51.91	49.86	73.98
Mount John	39	1507	11.24	5.02	55.58	46.65	34.40	16.97	59.23	48.11
Halley	595	37493	14.94	8.69	70.40	69.69	-6.46	-13.73	70.92	69.63
South Pole	981	190440	0.51	13.60	43.61	74.98	-26.36	-39.42	46.09	72.71
Jang Bogo	521	19688	-14.19	-13.98	50.94	40.38	-5.04	1.55	47.56	39.15
Arrival Heights	1757	226377	8.44	15.06	28.02	53.97	-2.97	-9.06	24.57	35.95
Scanning Doppler Imaging Fabry-Perot Interferometers (ground-based)										
Mawson	431	271124	4.99	-1.99	73.55	83.63	-2.69	-32.52	53.91	72.55
South Pole	72	156918	-5.17	19.25	58.30	81.82	-8.60	-23.80	47.08	68.16
McMurdo	253	290625	2.02	10.12	63.12	73.94	8.02	4.92	55.46	64.59
Space-based Instruments										
WINDII 557.7nm	477	169446	-6.89	-14.50	84.01	89.37	2.14	3.85	75.83	75.81
WINDII 630.0nm	121	6073	8.55	17.91	82.27	89.24	7.01	-13.10	77.57	76.98
GOCE	1256	102852	*-0.96*	*-53.55*	*38.95*	*77.03*	–	–	–	–

Figure 1.

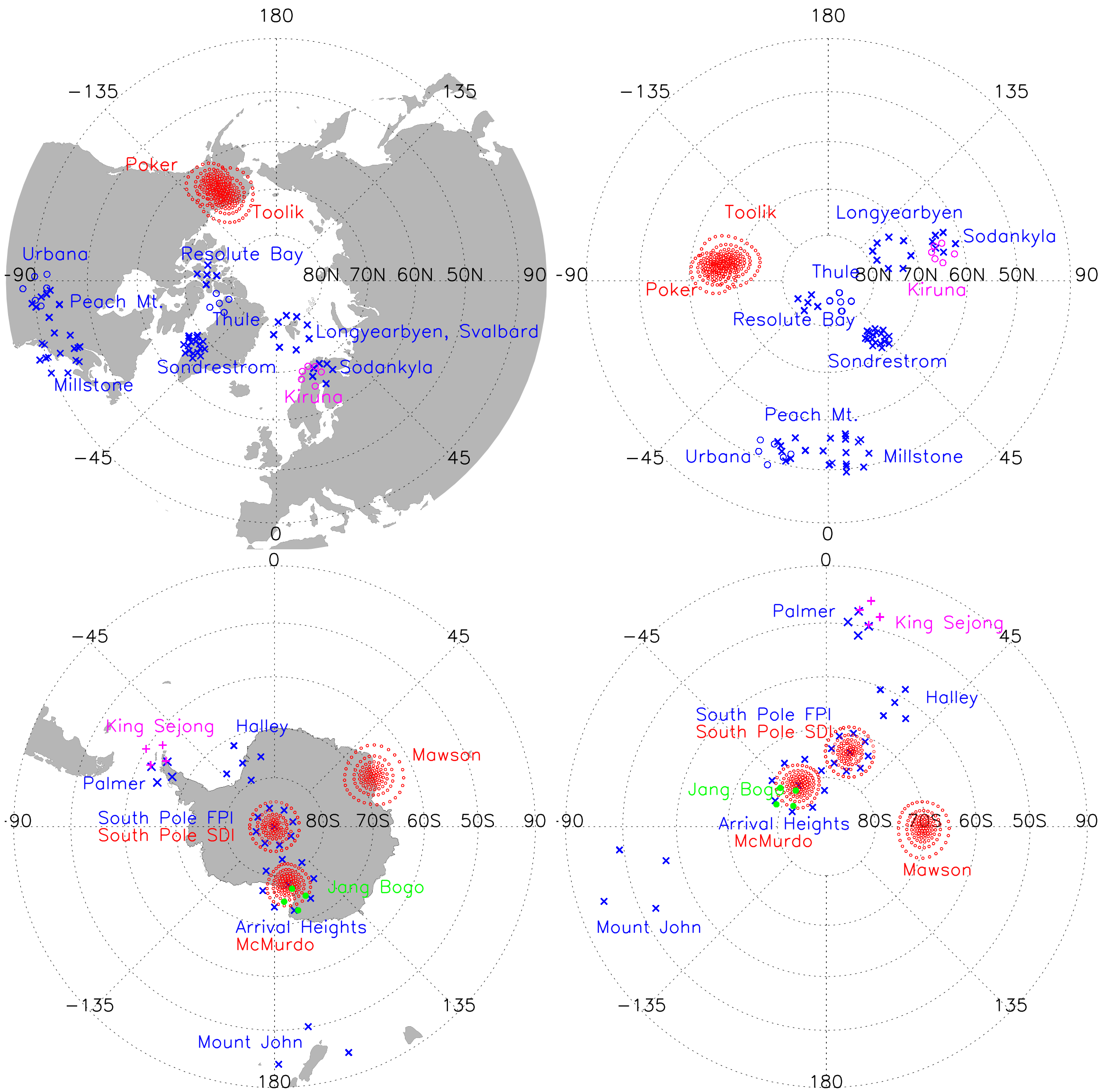
180
−135
135
Poker
Toolik
Urbana
Resolute Bay
-90
80N 70N 60N 50N
90
Peach Mt.
Thule
Longyearbyen, Svalbard
Sondrestrom
Sodankyla
Millstone
Kiruna
−45
45
0
180
−135
135
Toolik
Longyearbyen
Sodankyla
-90
Thule
80N 70N 60N 50N
90
Poker
Kiruna
Resolute Bay
Sondrestrom
Peach Mt.
−45
Urbana
Millstone
45
0
0
−45
45
King Sejong
Halley
Mawson
Palmer
South Pole FPI
South Pole SDI
-90
80S 70S 60S 50S
90
Jang Bogo
Arrival Heights
McMurdo
−135
135
Mount John
180
0
Palmer
King Sejong
−45
45
Halley
South Pole FPI
South Pole SDI
Jang Bogo
-90
Arrival Heights
80S 70S 60S 50S
90
McMurdo
Mawson
Mount John
−135
135
180

Figure 2.

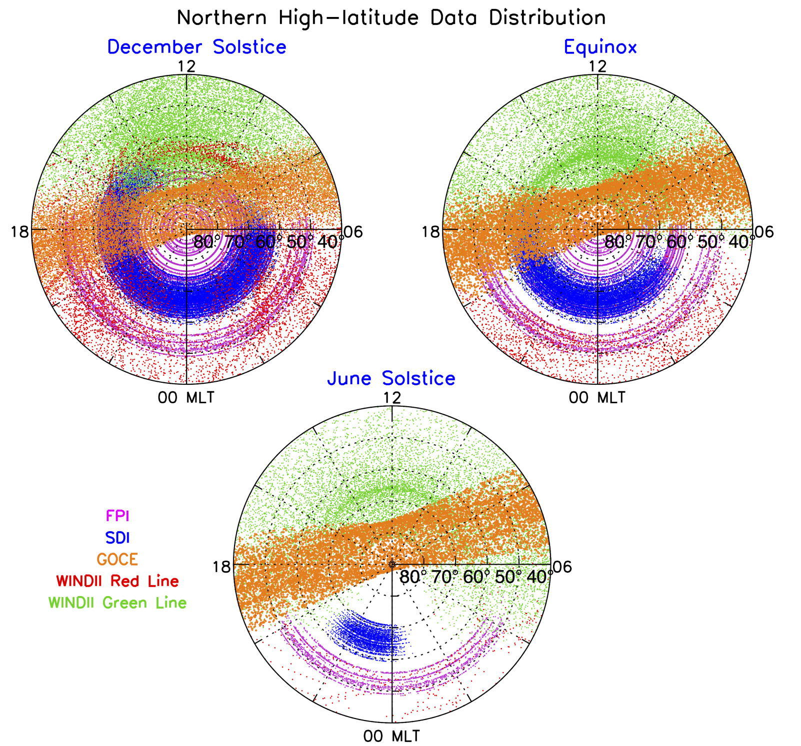
Northern High–latitude Data Distribution
December Solstice
Equinox
June Solstice
12
18
06
00 MLT
80° 70° 60° 50° 40°
FPI
SDI
GOCE
WINDII Red Line
WINDII Green Line

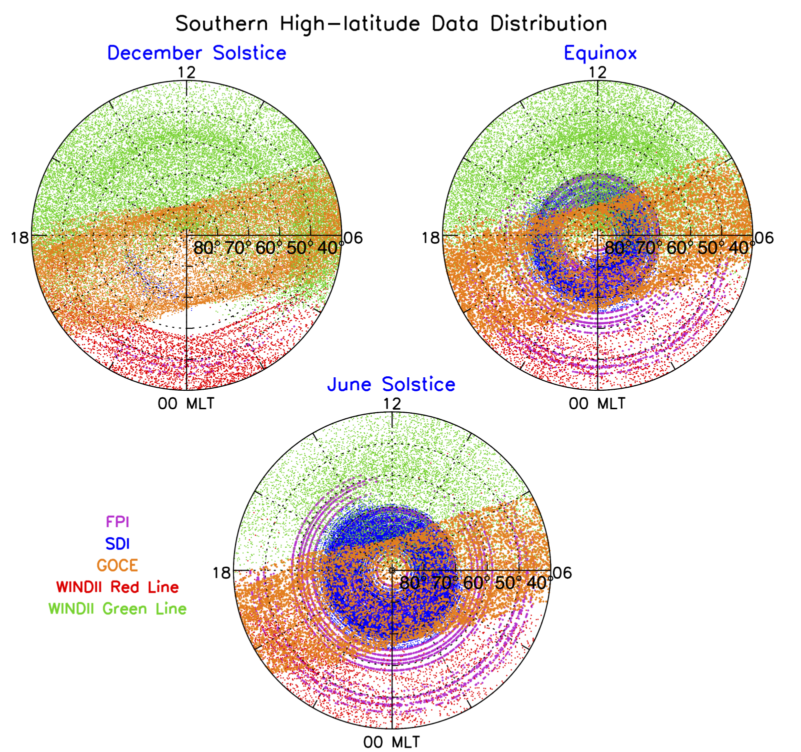
Southern High–latitude Data Distribution
December Solstice
Equinox
June Solstice
12
18
06
00 MLT
80° 70° 60° 50° 40°
FPI
SDI
GOCE
WINDII Red Line
WINDII Green Line

Figure 3.

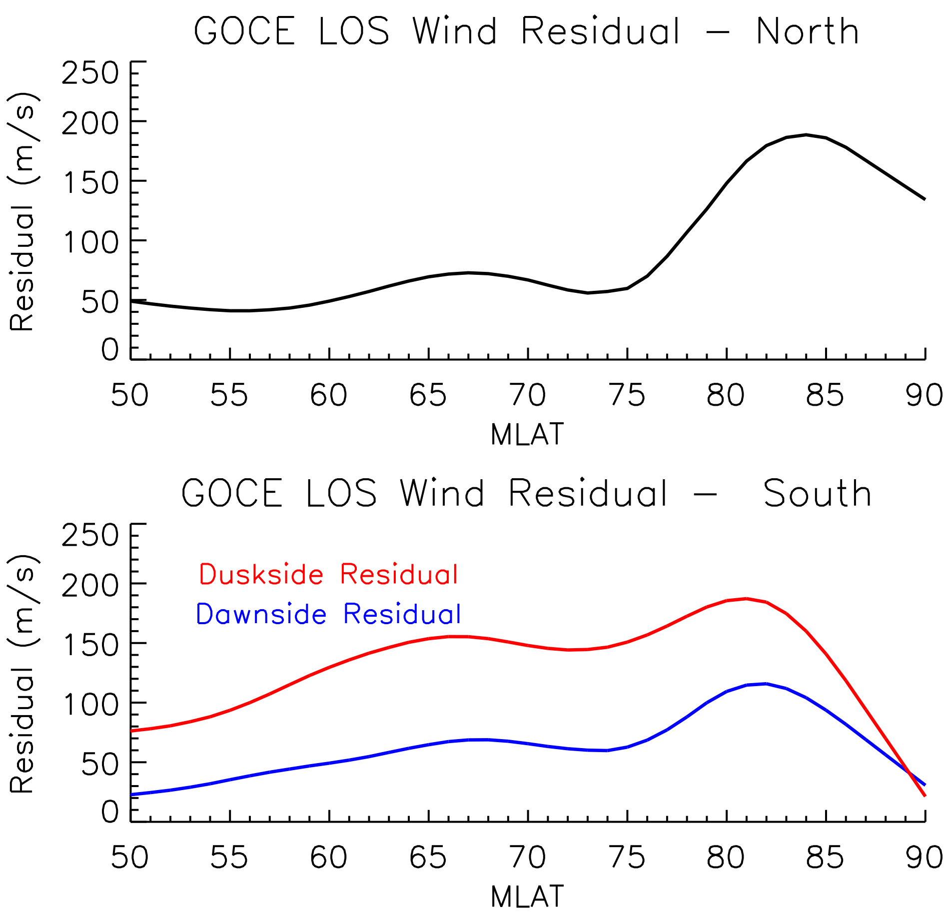
GOCE LOS Wind Residual – North
Residual (m/s)
250
200
150
100
50
0
50
55
60
65
70
75
80
85
90
MLAT
GOCE LOS Wind Residual – South
Residual (m/s)
Duskside Residual
Dawnside Residual
250
200
150
100
50
0
50
55
60
65
70
75
80
85
90
MLAT

Figure 4.

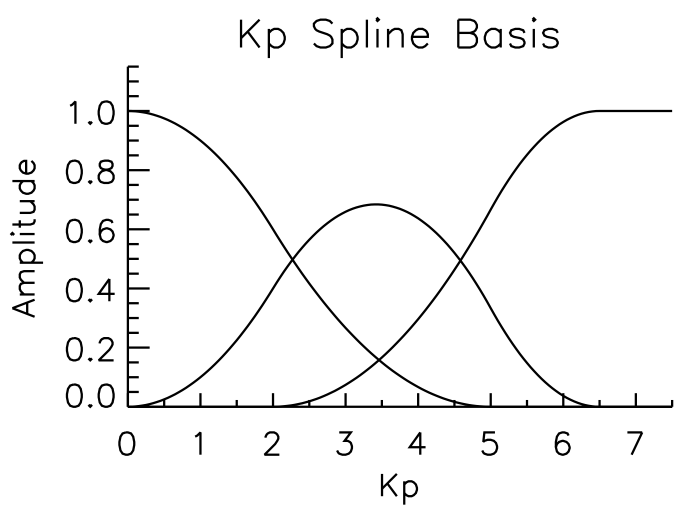
Kp Spline Basis
1.0
0.8
0.6
0.4
0.2
0.0
Amplitude
0
1
2
3
4
5
6
7
Kp

Figure 5.

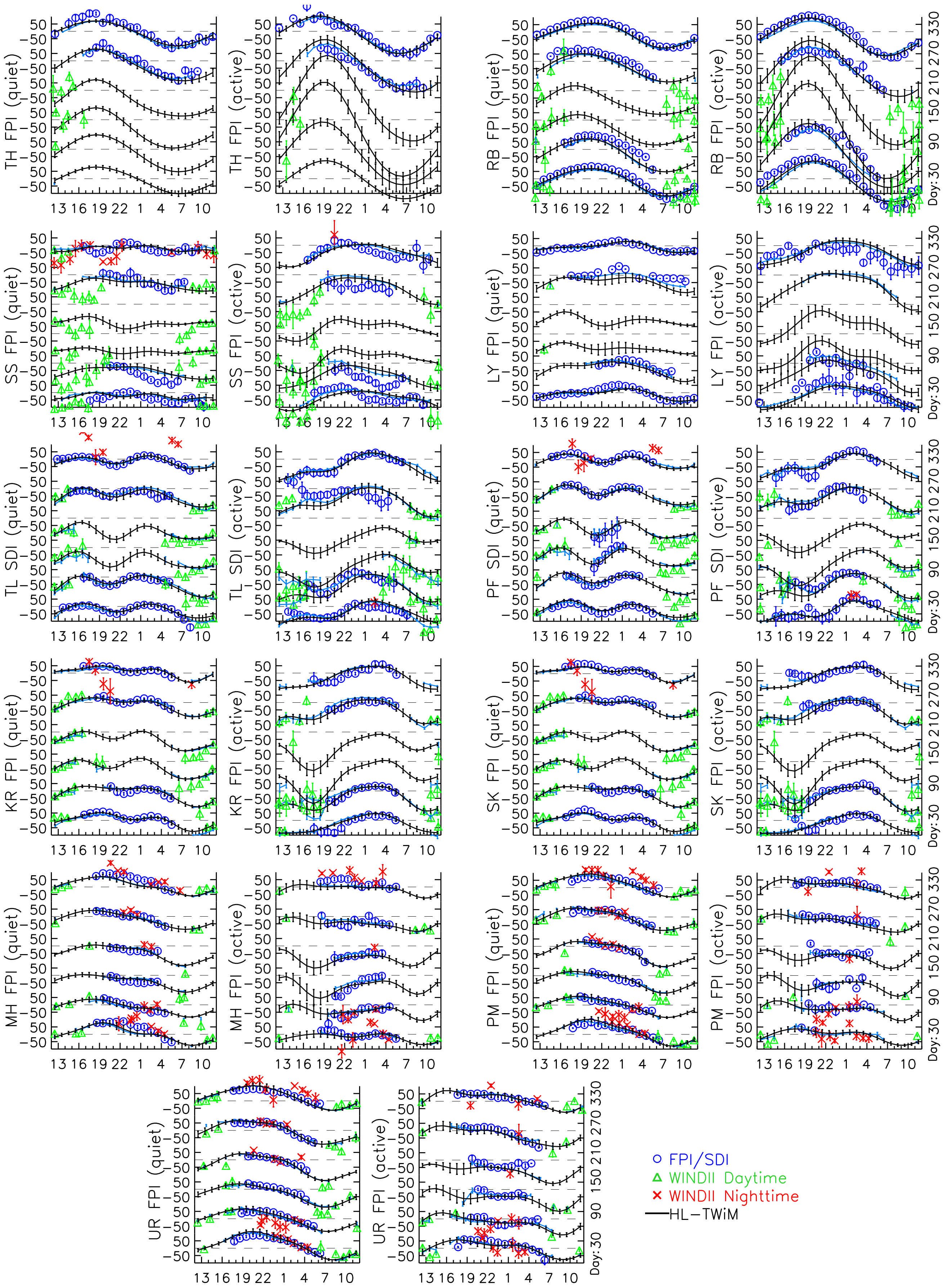

TH FPI (quiet)
TH FPI (active)
RB FPI (quiet)
RB FPI (active)
SS FPI (quiet)
SS FPI (active)
LY FPI (quiet)
LY FPI (active)
TL SDI (quiet)
TL SDI (active)
PF SDI (quiet)
PF SDI (active)
KR FPI (quiet)
KR FPI (active)
SK FPI (quiet)
SK FPI (active)
MH FPI (quiet)
MH FPI (active)
PM FPI (quiet)
PM FPI (active)
UR FPI (quiet)
UR FPI (active)
13 16 19 22 1 4 7 10
MLT
Day:30 90 150 210 270 330
FPI/SDI
WINDII Daytime
WINDII Nighttime
HL−TWiM

Figure 6.

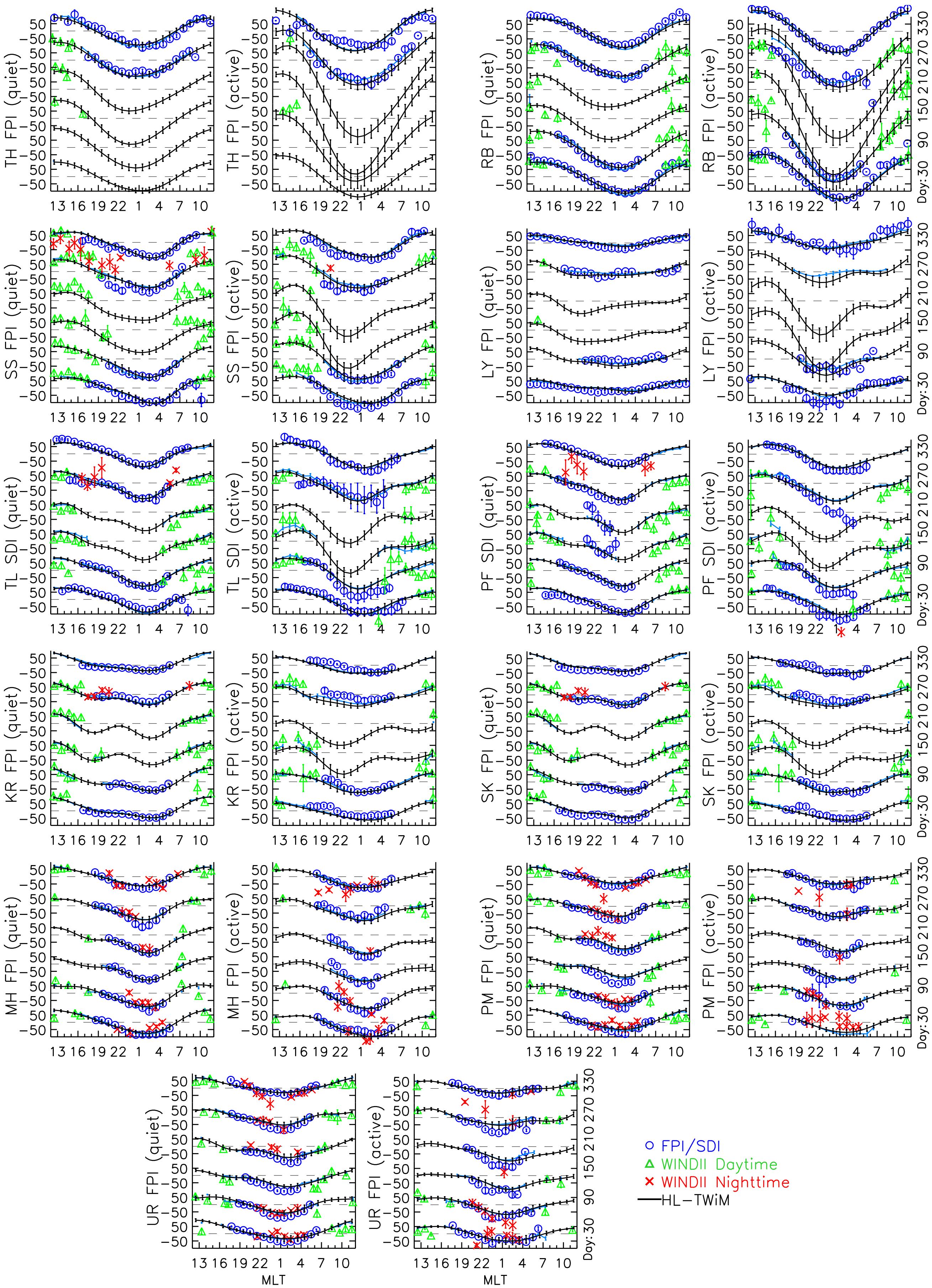
TH FPI (quiet)
TH FPI (active)
RB FPI (quiet)
RB FPI (active)
SS FPI (quiet)
SS FPI (active)
LY FPI (quiet)
LY FPI (active)
TL SDI (quiet)
TL SDI (active)
PF SDI (quiet)
PF SDI (active)
KR FPI (quiet)
KR FPI (active)
SK FPI (quiet)
SK FPI (active)
MH FPI (quiet)
MH FPI (active)
PM FPI (quiet)
PM FPI (active)
UR FPI (quiet)
UR FPI (active)
13 16 19 22 1 4 7 10
MLT
Day: 30 90 150 210 270 330
FPI/SDI
WINDII Daytime
WINDII Nighttime
HL−TWiM

Figure 7.

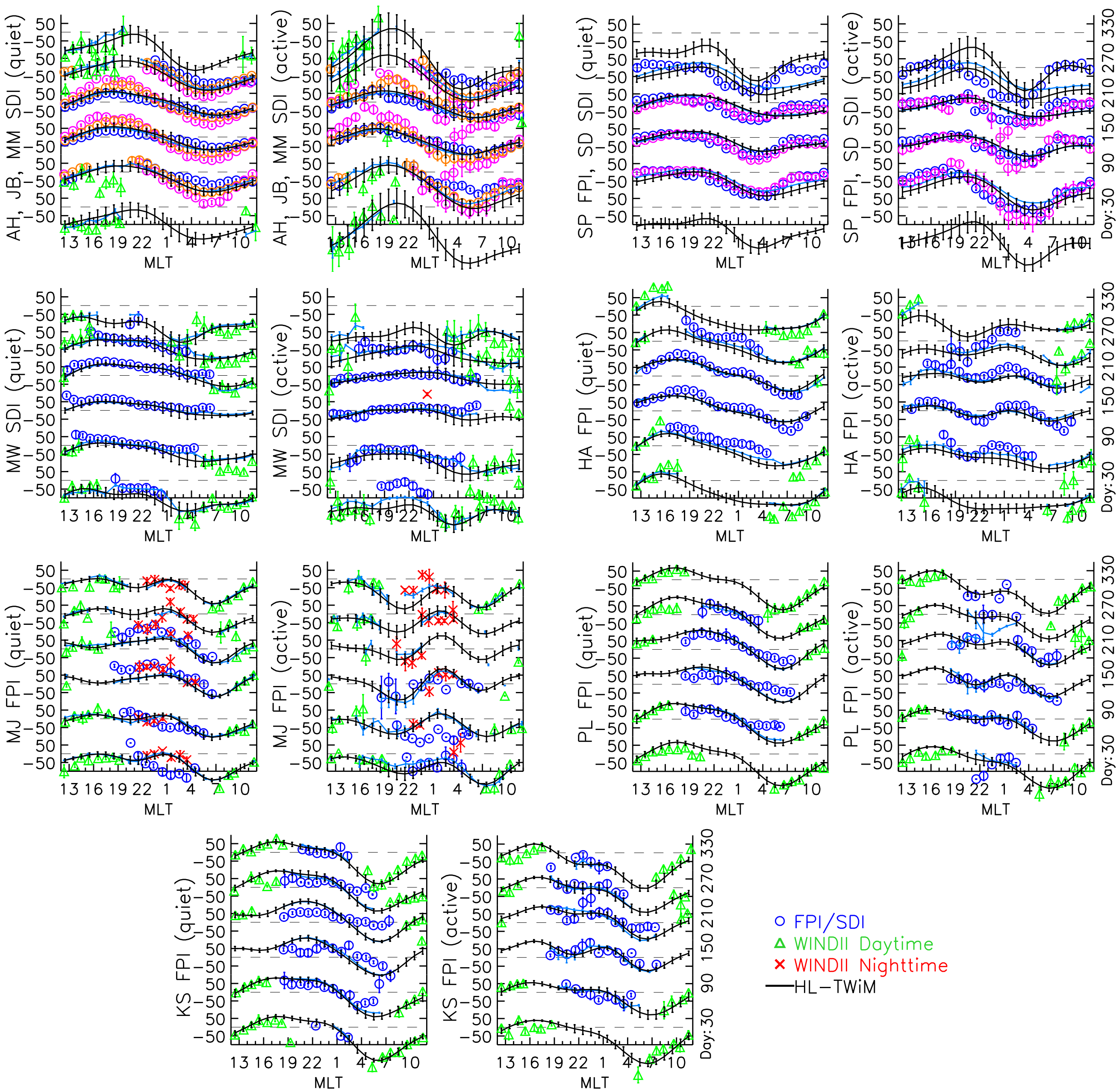
AH, JB, MM SDI (quiet)
AH, JB, MM SDI (active)
SP FPI, SD SDI (quiet)
SP FPI, SD SDI (active)
MW SDI (quiet)
MW SDI (active)
HA FPI (quiet)
HA FPI (active)
MJ FPI (quiet)
MJ FPI (active)
PL FPI (quiet)
PL FPI (active)
KS FPI (quiet)
KS FPI (active)
MLT
Day:30 90 150 210 270 330
FPI/SDI
WINDII Daytime
WINDII Nighttime
HL−TWiM

Figure 8.

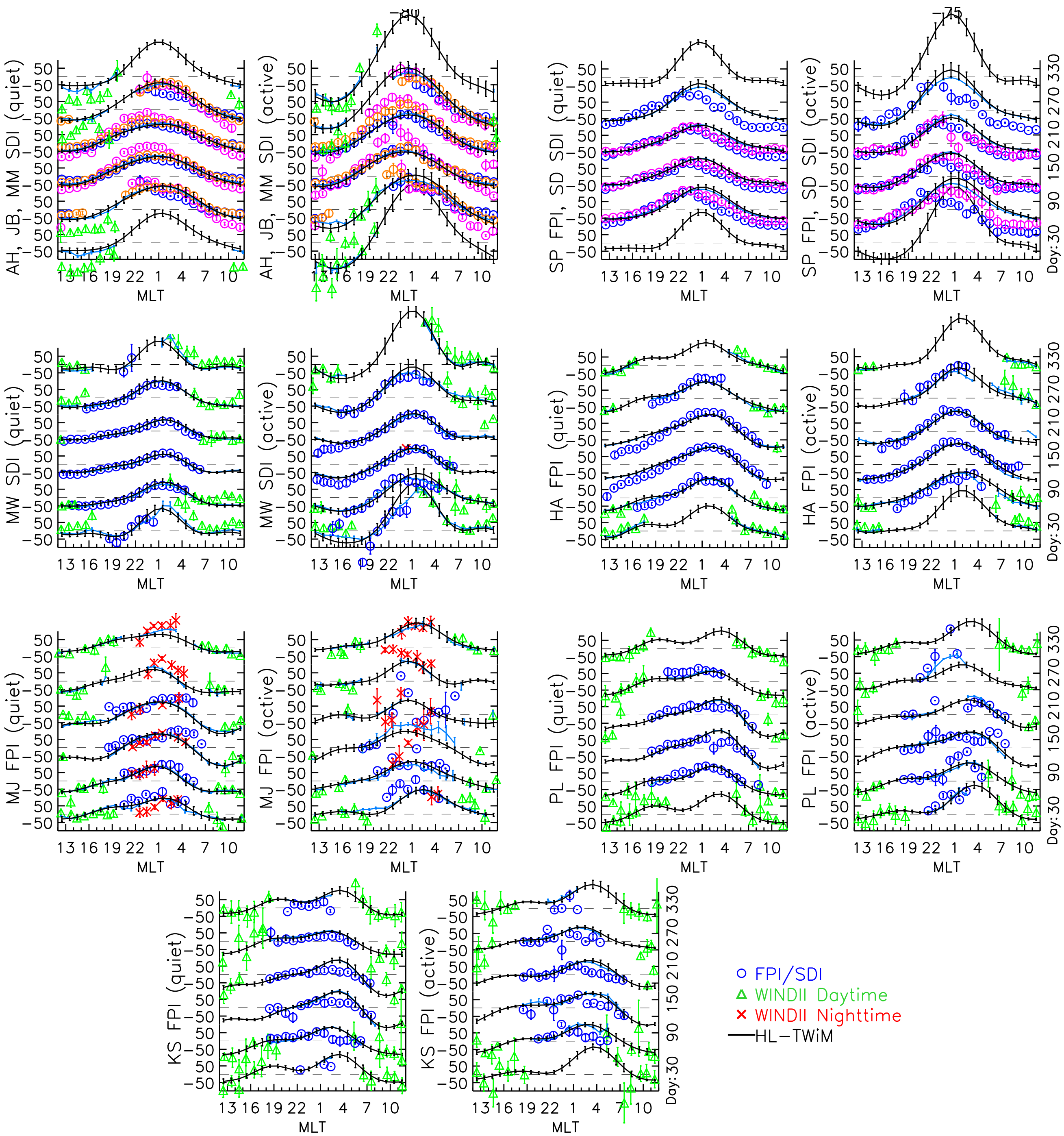
AH, JB, MM SDI (quiet)
AH, JB, MM SDI (active)
SP FPI, SD SDI (quiet)
SP FPI, SD SDI (active)
MW SDI (quiet)
MW SDI (active)
HA FPI (quiet)
HA FPI (active)
MJ FPI (quiet)
MJ FPI (active)
PL FPI (quiet)
PL FPI (active)
KS FPI (quiet)
KS FPI (active)
MLT
Day:30 90 150 210 270 330
FPI/SDI
WINDII Daytime
WINDII Nighttime
HL−TWiM

Figure 9.

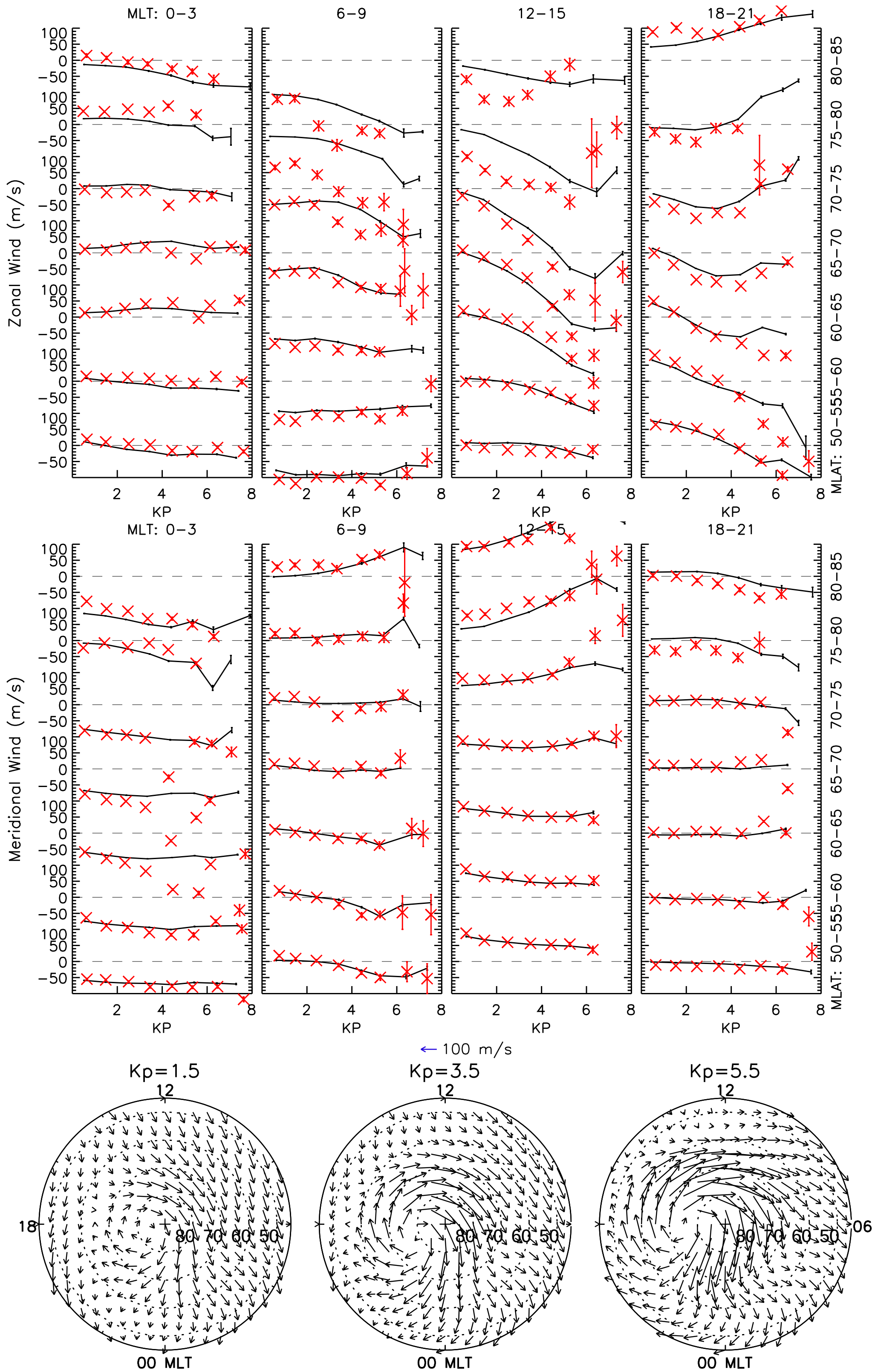
MLT: 0-3
6-9
12-15
18-21
Zonal Wind (m/s)
Meridional Wind (m/s)
KP
MLAT: 50-55
55-60
60-65
65-70
70-75
75-80
80-85
100 m/s
Kp=1.5
Kp=3.5
Kp=5.5
12
18
06
00 MLT
80
70
60
50

Figure 10.

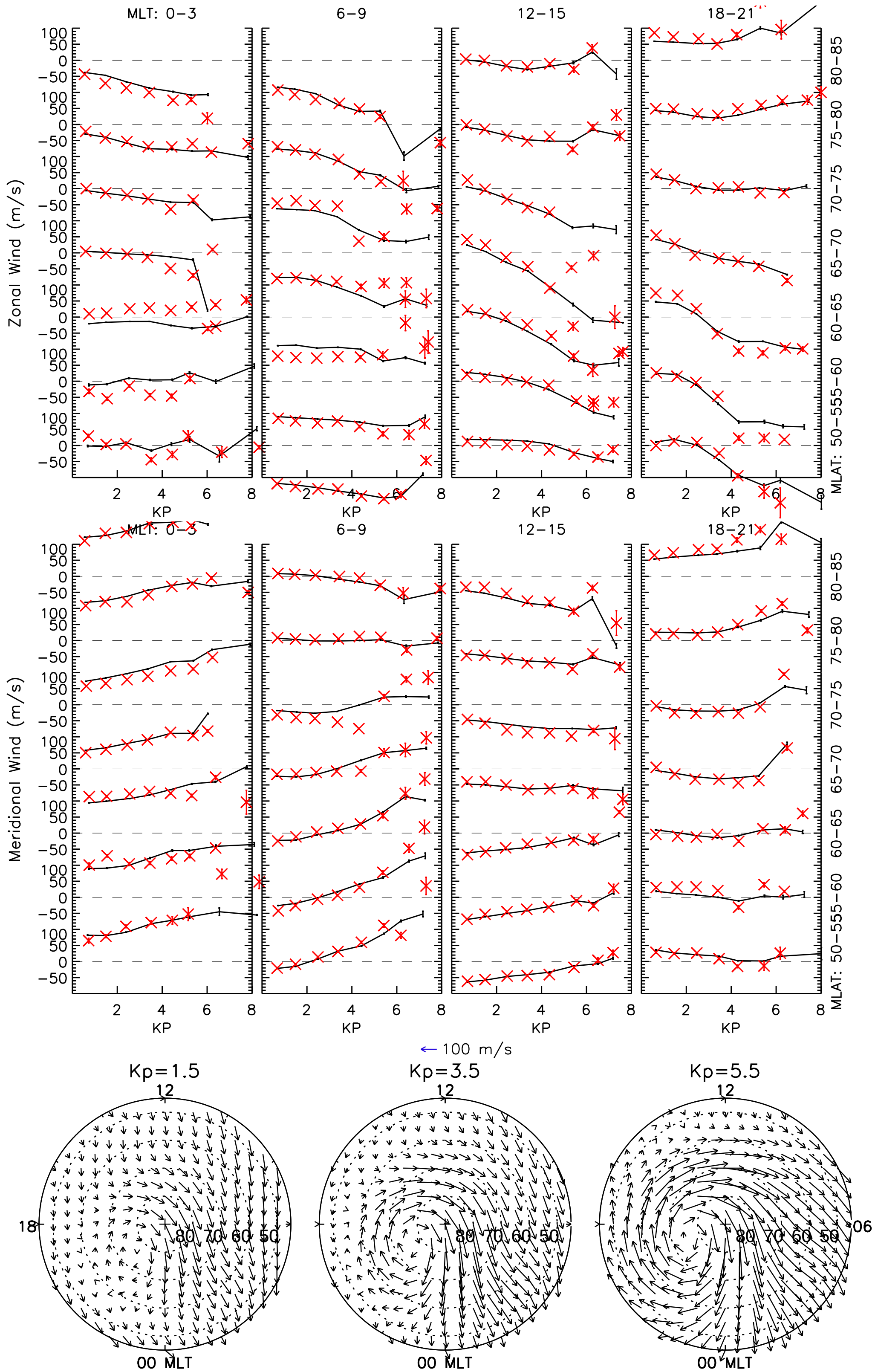

MLT: 0-3
6-9
12-15
18-21
Zonal Wind (m/s)
Meridional Wind (m/s)
KP
MLAT: 50-55
55-60
60-65
65-70
70-75
75-80
80-85
← 100 m/s
Kp=1.5
Kp=3.5
Kp=5.5
12
18
06
00 MLT
80
70
60
50

Figure 11.

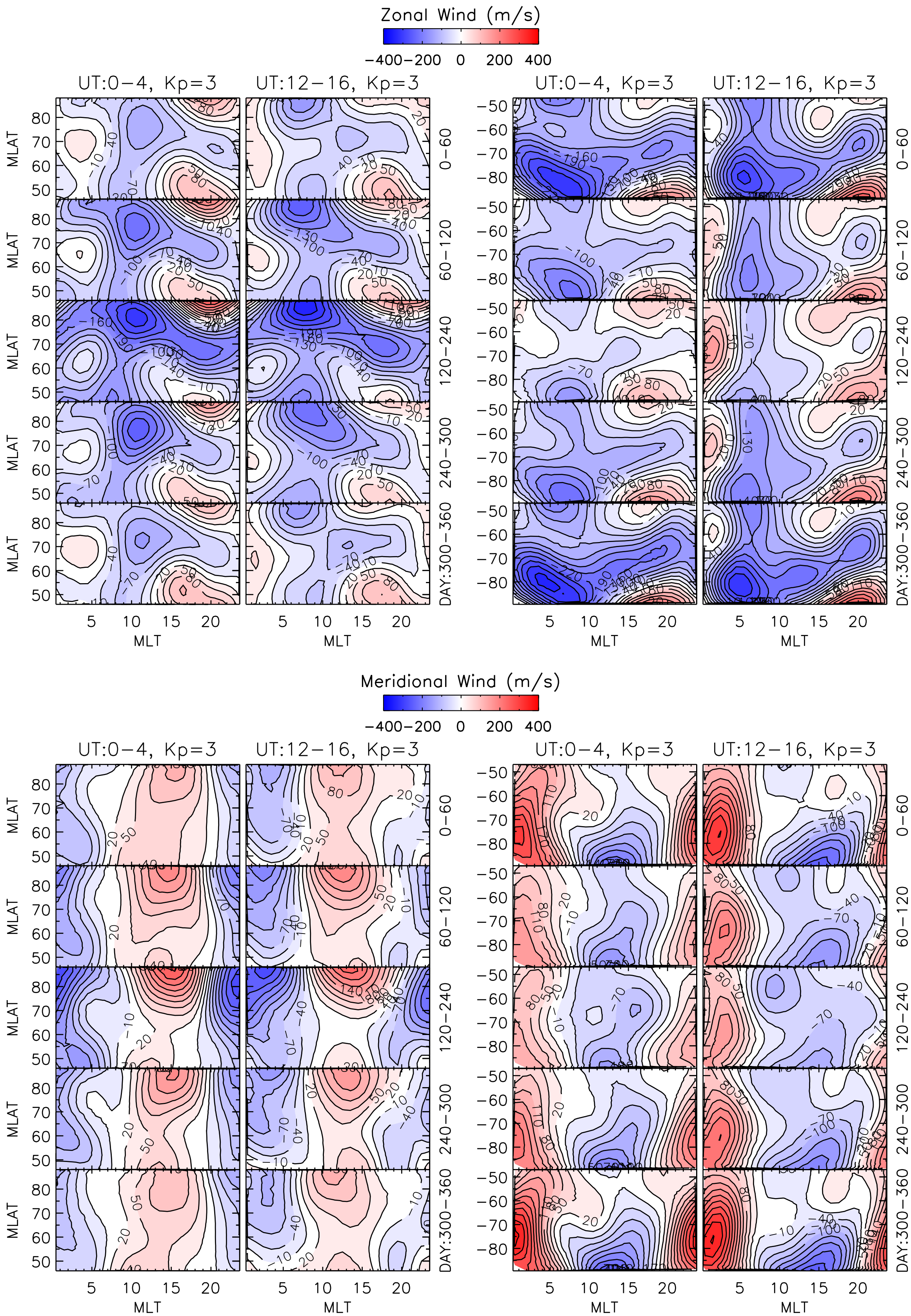
Zonal Wind (m/s)
−400 −200 0 200 400
UT:0−4, Kp=3
UT:12−16, Kp=3
UT:0−4, Kp=3
UT:12−16, Kp=3
MLAT
MLT
0−60
60−120
120−240
240−300
DAY:300−360
Meridional Wind (m/s)
−400 −200 0 200 400
UT:0−4, Kp=3
UT:12−16, Kp=3
UT:0−4, Kp=3
UT:12−16, Kp=3
MLAT
MLT
0−60
60−120
120−240
240−300
DAY:300−360

Figure 12.

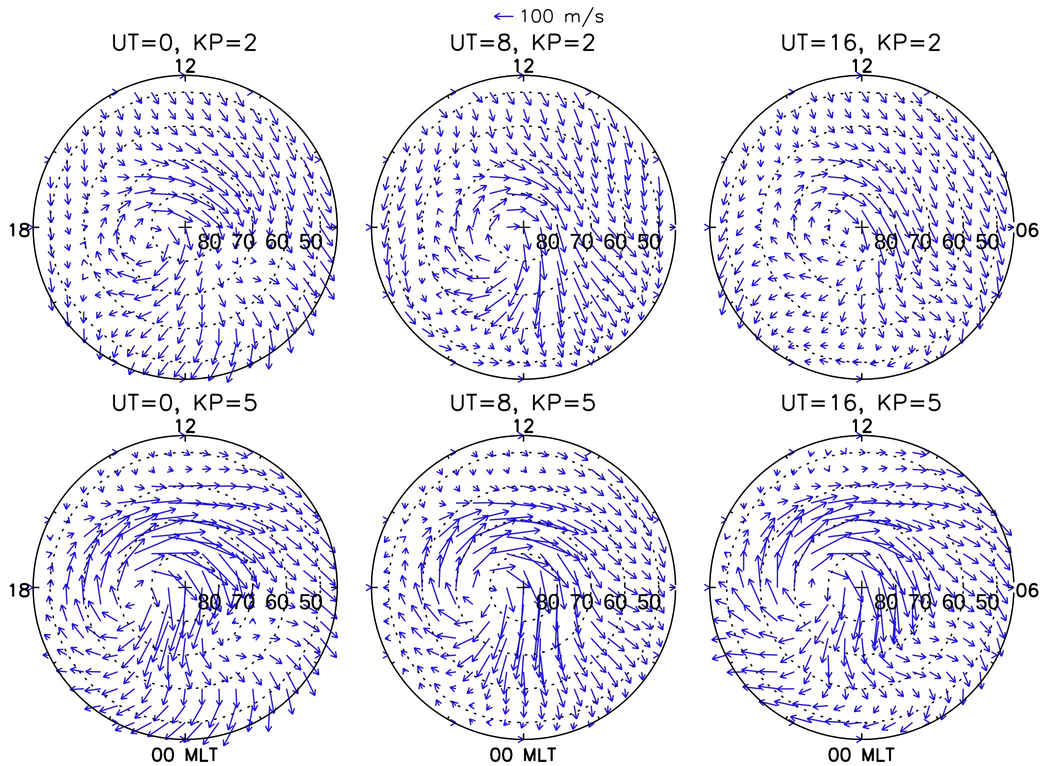

100 m/s
UT=0, KP=2
UT=8, KP=2
UT=16, KP=2
UT=0, KP=5
UT=8, KP=5
UT=16, KP=5
12
18
06
80 70 60 50
00 MLT

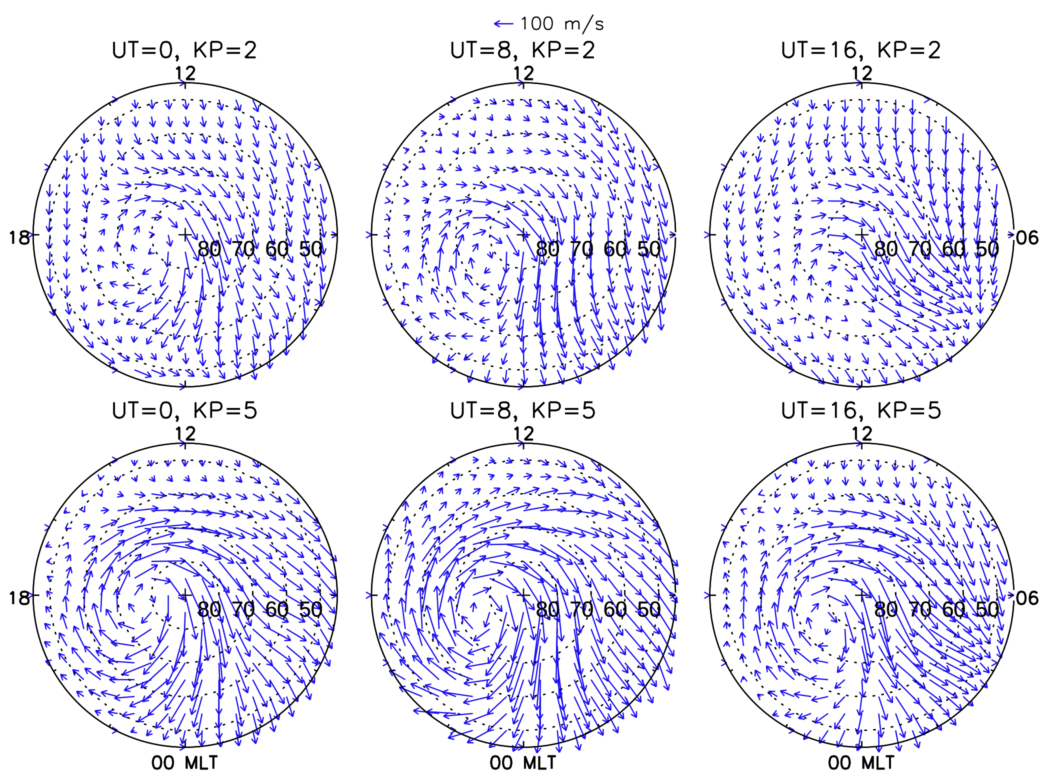

100 m/s
UT=0, KP=2
UT=8, KP=2
UT=16, KP=2
UT=0, KP=5
UT=8, KP=5
UT=16, KP=5
12
18
06
80 70 60 50
00 MLT

Figure 13.

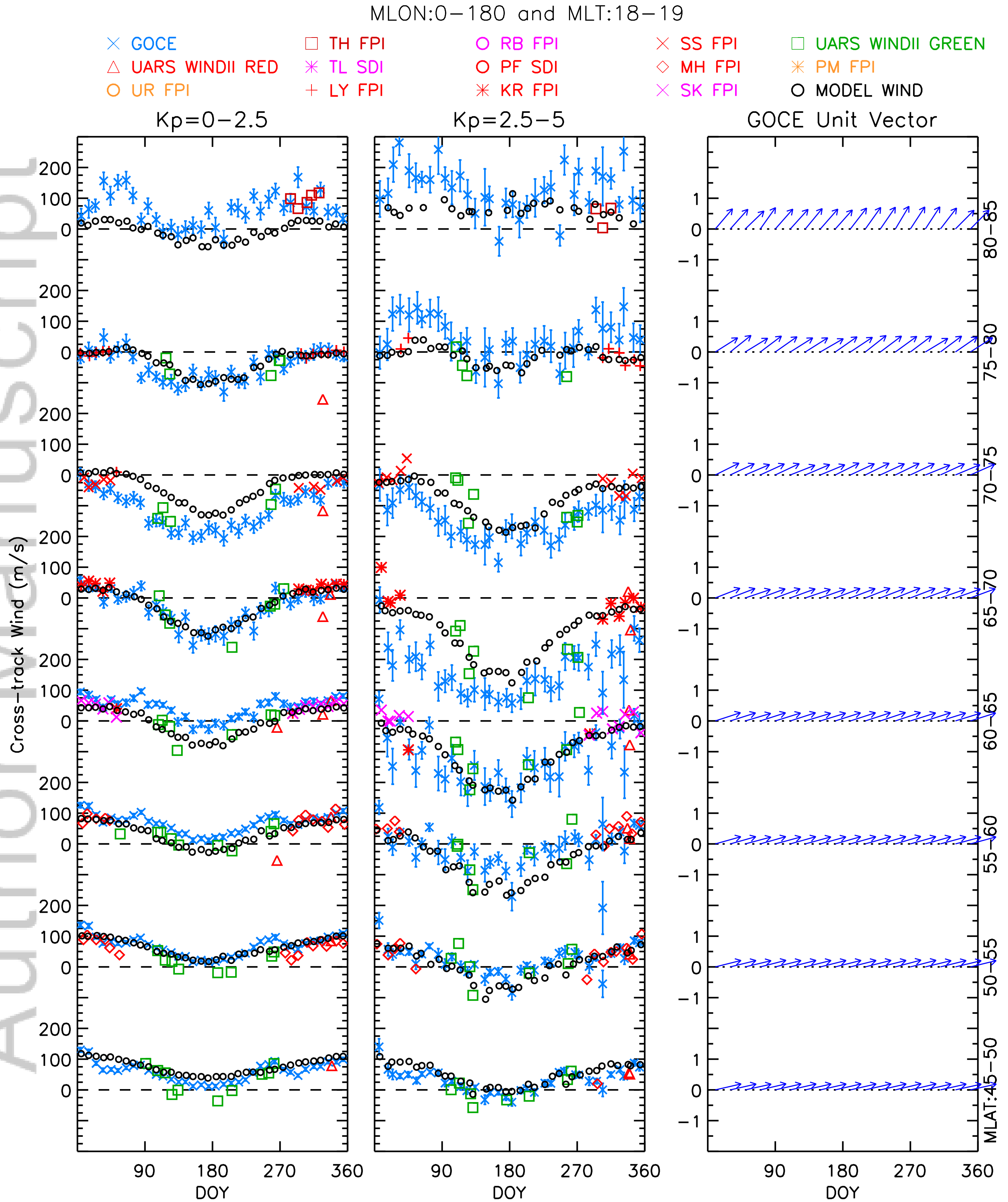

MLON:0−180 and MLT:18−19
GOCE
TH FPI
RB FPI
SS FPI
UARS WINDII GREEN
UARS WINDII RED
TL SDI
PF SDI
MH FPI
PM FPI
UR FPI
LY FPI
KR FPI
SK FPI
MODEL WIND
Kp=0−2.5
Kp=2.5−5
GOCE Unit Vector
Cross−track Wind (m/s)
DOY
MLAT:45−50
50−55
55−60
60−65
65−70
70−75
75−80
80−85

Figure 14.

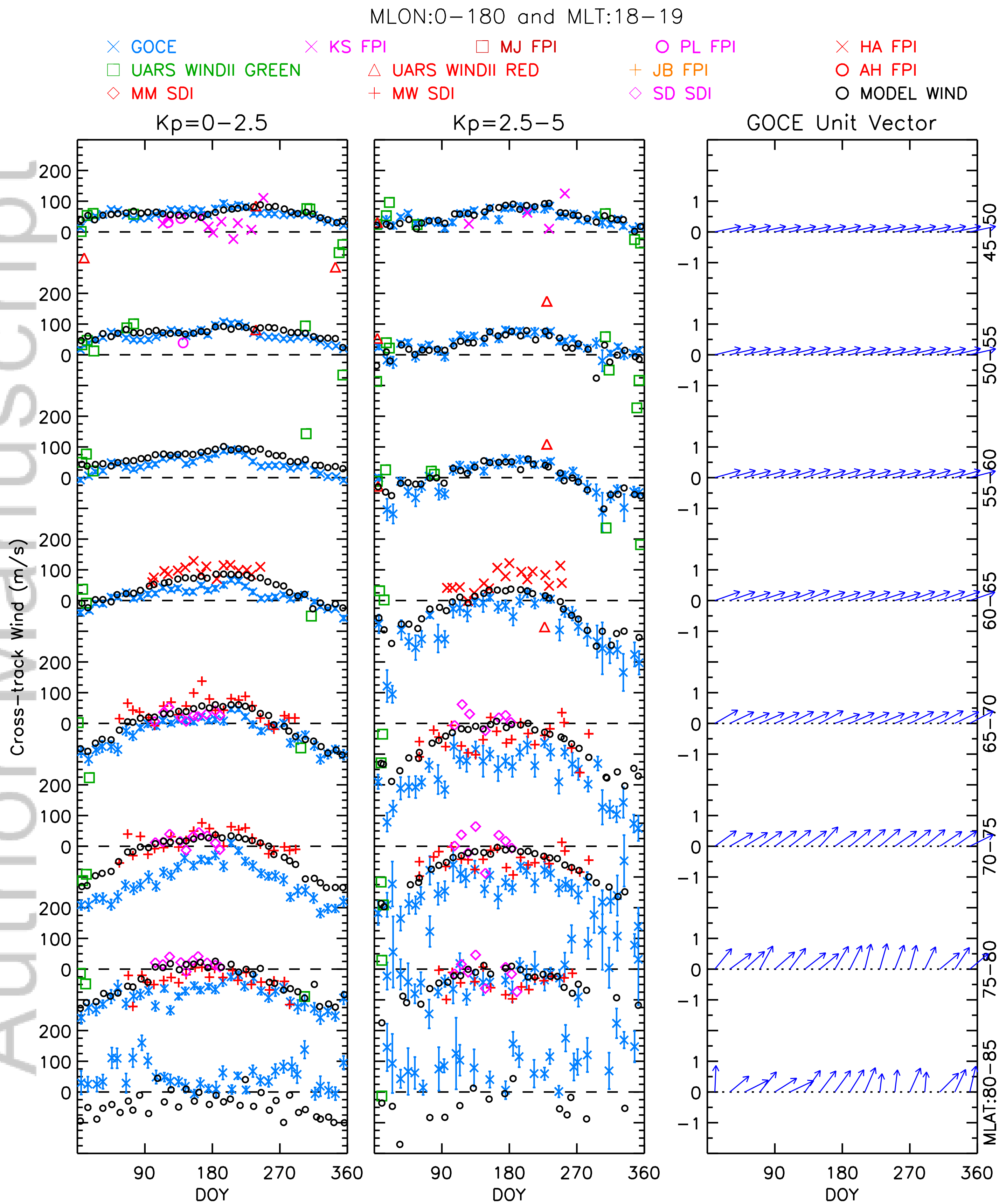
MLON:0−180 and MLT:18−19
GOCE
KS FPI
MJ FPI
PL FPI
HA FPI
UARS WINDII GREEN
UARS WINDII RED
JB FPI
AH FPI
MM SDI
MW SDI
SD SDI
MODEL WIND
Kp=0−2.5
Kp=2.5−5
GOCE Unit Vector
Cross−track Wind (m/s)
DOY
45−50
50−55
55−60
60−65
65−70
70−75
75−80
MLAT:80−85

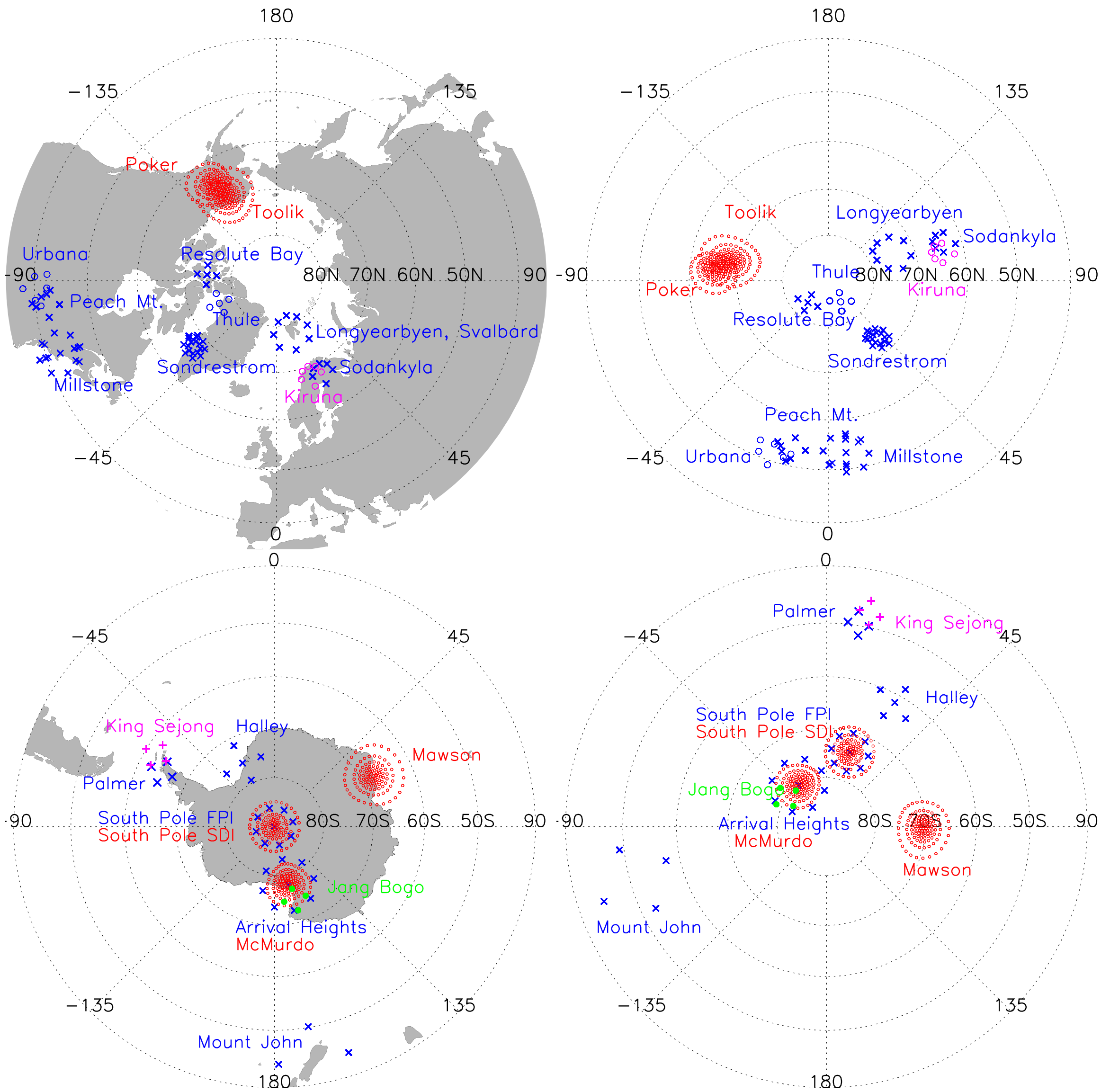
180
-135
135
-90
90
-45
45
0
80N 70N 60N 50N
80S 70S 60S 50S
Poker
Toolik
Urbana
Resolute Bay
Peach Mt.
Thule
Longyearben, Svalbard
Longyearbyen
Sondrestrom
Sodankyla
Millstone
Kiruna
King Sejong
Halley
Palmer
Mawson
South Pole FPI
South Pole SDI
Jang Bogo
Arrival Heights
McMurdo
Mount John

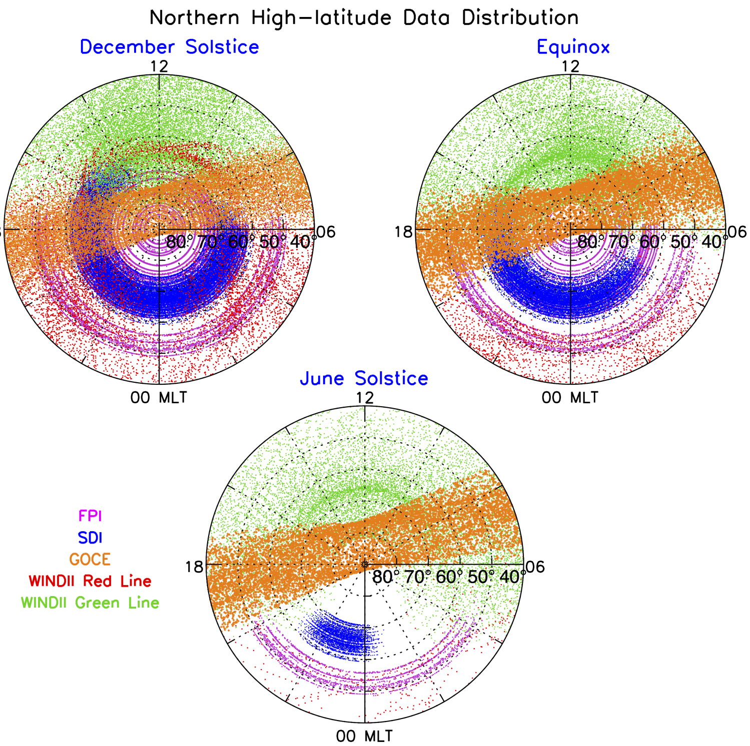
Northern High-latitude Data Distribution
December Solstice
Equinox
June Solstice
12
18
06
00 MLT
80° 70° 60° 50° 40°
FPI
SDI
GOCE
WINDII Red Line
WINDII Green Line

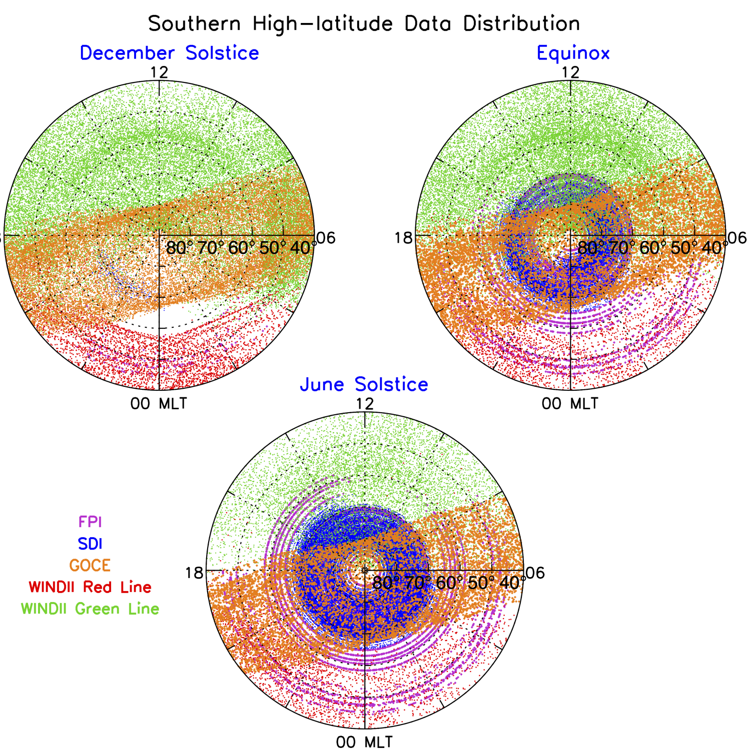
Southern High-latitude Data Distribution
December Solstice
Equinox
June Solstice
12
18
06
00 MLT
80° 70° 60° 50° 40°
FPI
SDI
GOCE
WINDII Red Line
WINDII Green Line

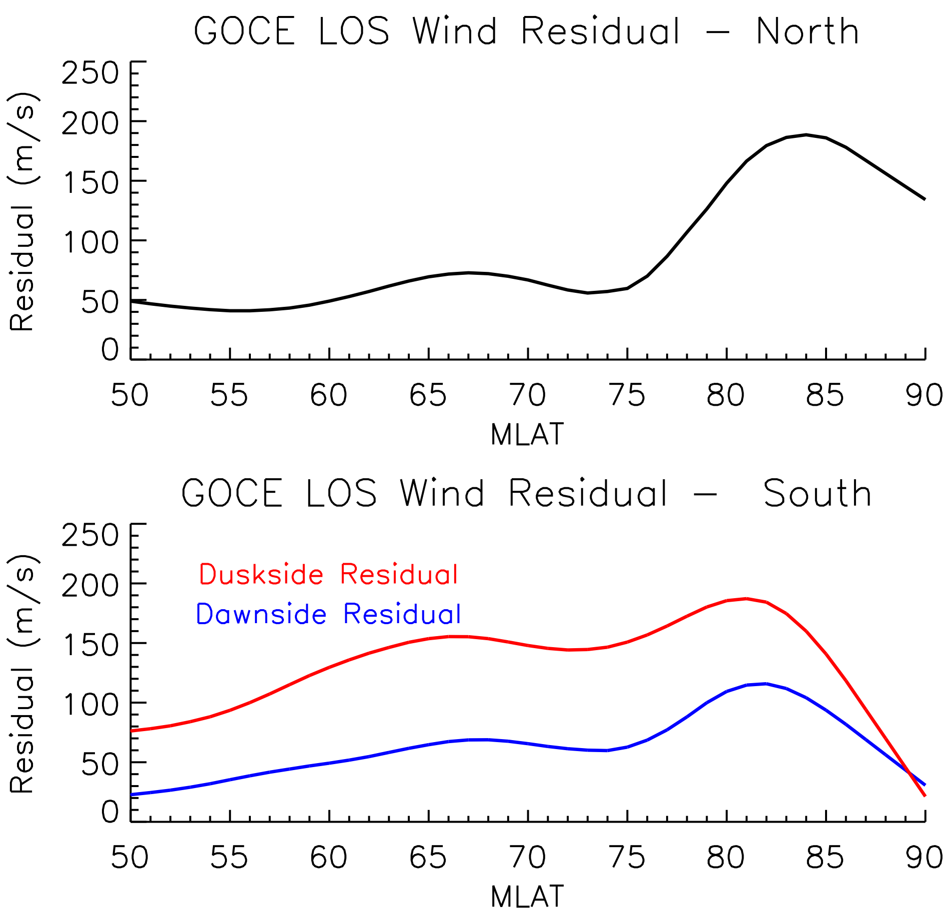

GOCE LOS Wind Residual – North
Residual (m/s)
MLAT
GOCE LOS Wind Residual – South
Duskside Residual
Dawnside Residual
Residual (m/s)
MLAT

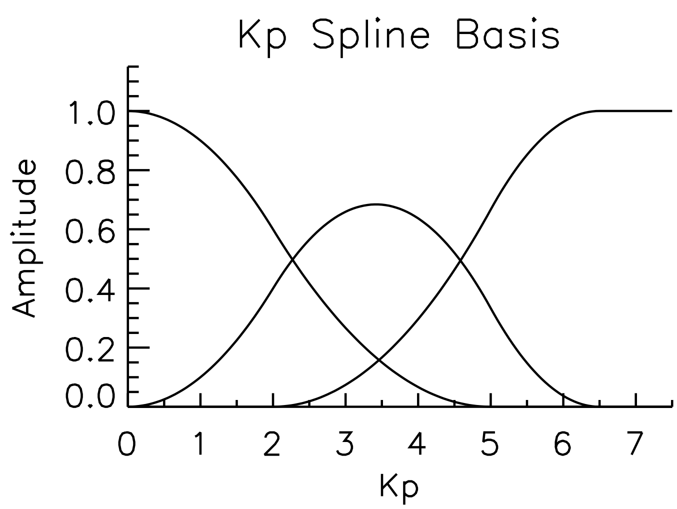
Kp Spline Basis
Amplitude
1.0
0.8
0.6
0.4
0.2
0.0
0
1
2
3
4
5
6
7
Kp

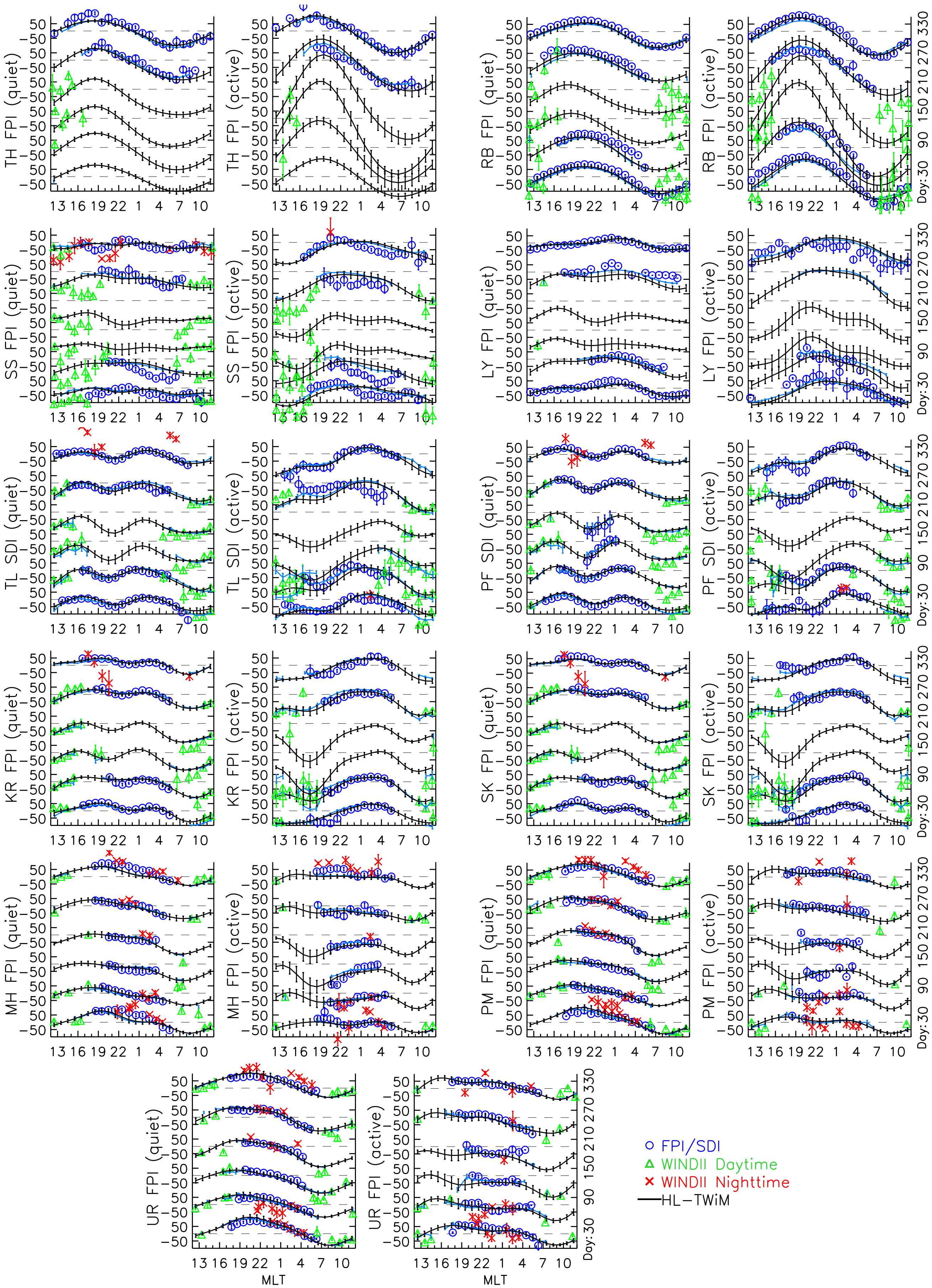
TH FPI (quiet)
TH FPI (active)
RB FPI (quiet)
RB FPI (active)
SS FPI (quiet)
SS FPI (active)
LY FPI (quiet)
LY FPI (active)
TL SDI (quiet)
TL SDI (active)
PF SDI (quiet)
PF SDI (active)
KR FPI (quiet)
KR FPI (active)
SK FPI (quiet)
SK FPI (active)
MH FPI (quiet)
MH FPI (active)
PM FPI (quiet)
PM FPI (active)
UR FPI (quiet)
UR FPI (active)
13 16 19 22 1 4 7 10
MLT
Day:30 90 150 210 270 330
FPI/SDI
WINDII Daytime
WINDII Nighttime
HL−TWiM

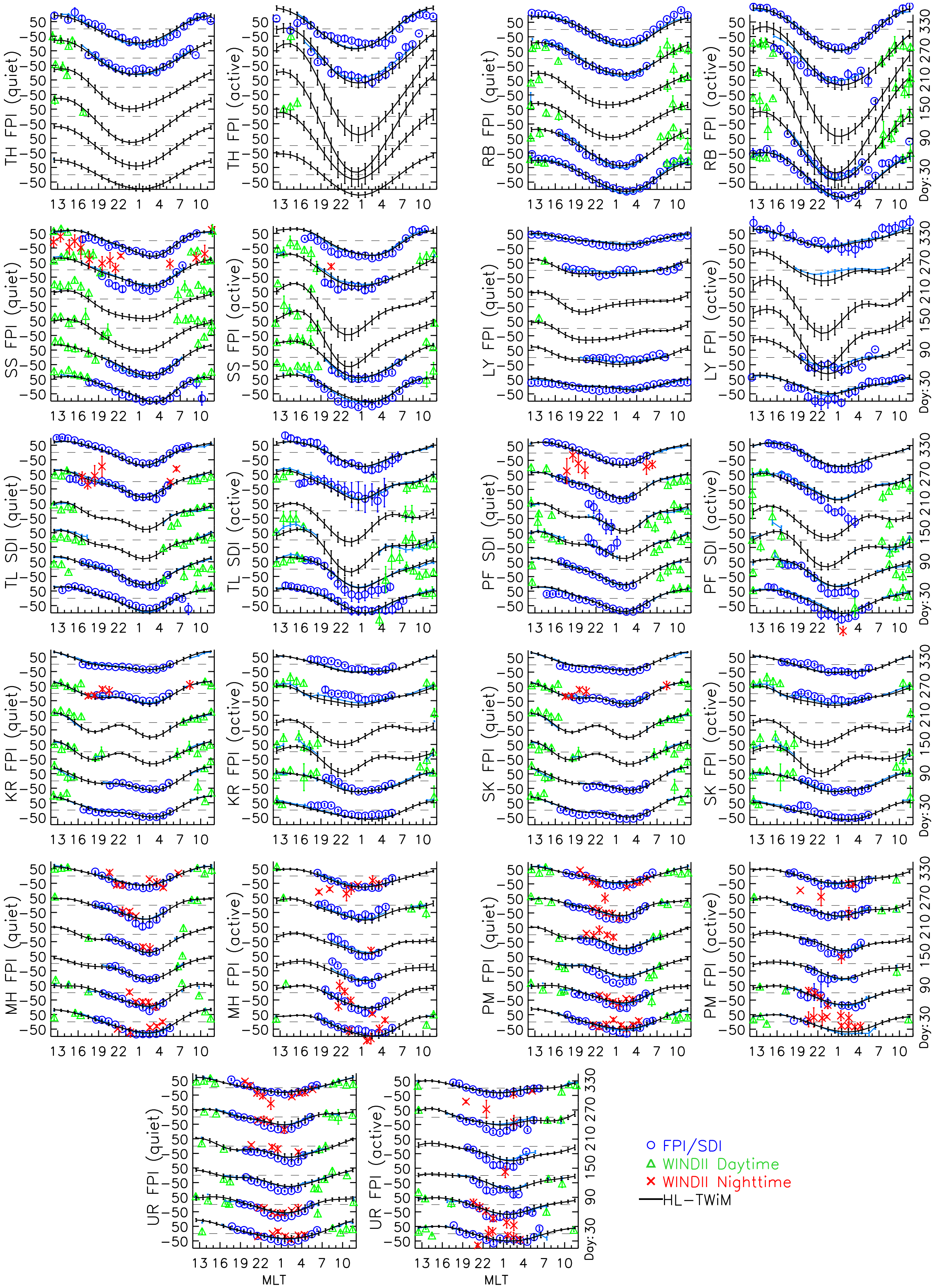
TH FPI (quiet)
TH FPI (active)
RB FPI (quiet)
RB FPI (active)
SS FPI (quiet)
SS FPI (active)
LY FPI (quiet)
LY FPI (active)
TL SDI (quiet)
TL SDI (active)
PF SDI (quiet)
PF SDI (active)
KR FPI (quiet)
KR FPI (active)
SK FPI (quiet)
SK FPI (active)
MH FPI (quiet)
MH FPI (active)
PM FPI (quiet)
PM FPI (active)
UR FPI (quiet)
UR FPI (active)
MLT
Day: 30 90 150 210 270 330
FPI/SDI
WINDII Daytime
WINDII Nighttime
HL−TWiM

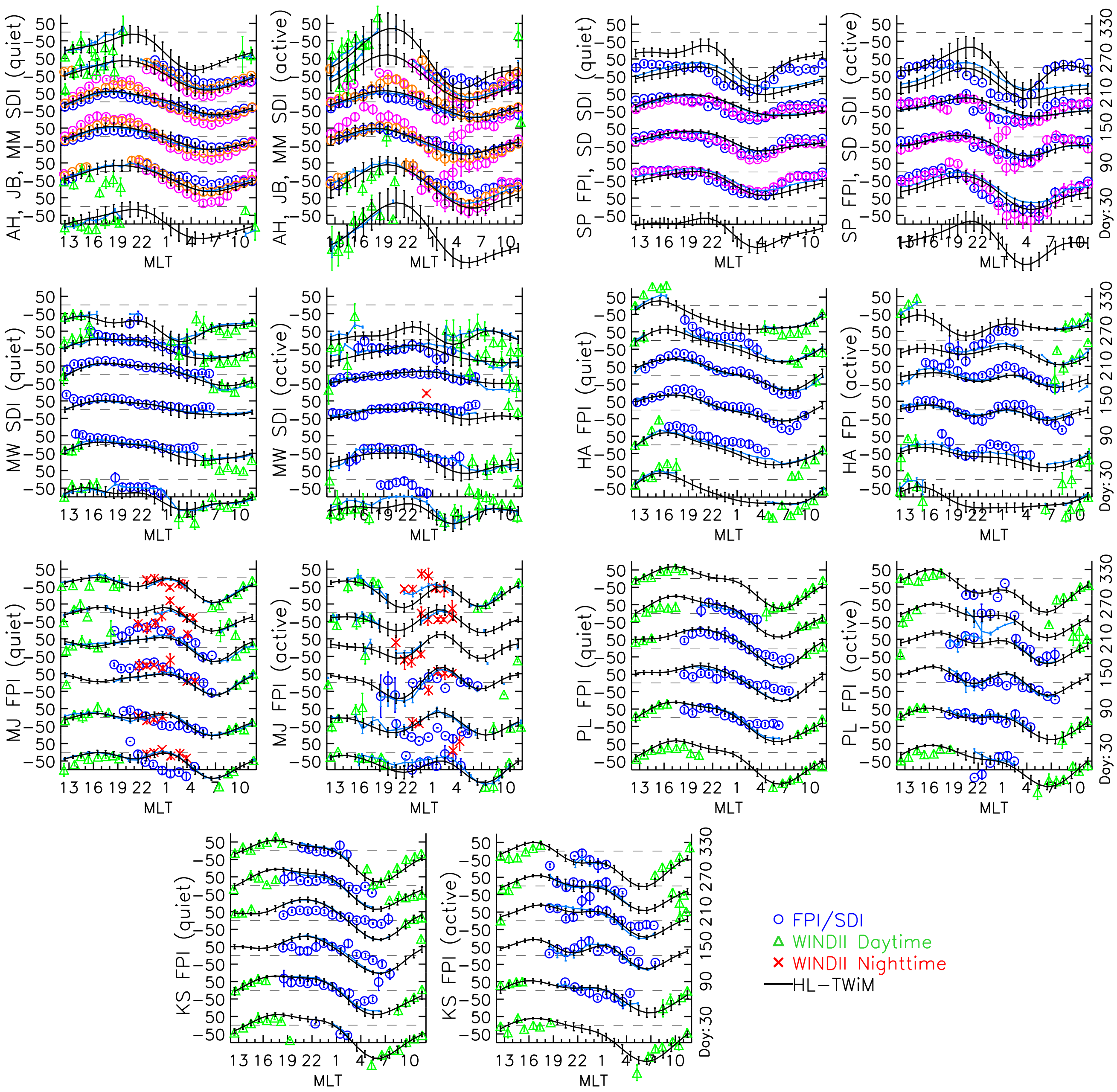

AH, JB, MM SDI (quiet)
AH, JB, MM SDI (active)
SP FPI, SD SDI (quiet)
SP FPI, SD SDI (active)
MW SDI (quiet)
MW SDI (active)
HA FPI (quiet)
HA FPI (active)
MJ FPI (quiet)
MJ FPI (active)
PL FPI (quiet)
PL FPI (active)
KS FPI (quiet)
KS FPI (active)
MLT
Day: 30 90 150 210 270 330
FPI/SDI
WINDII Daytime
WINDII Nighttime
HL−TWiM

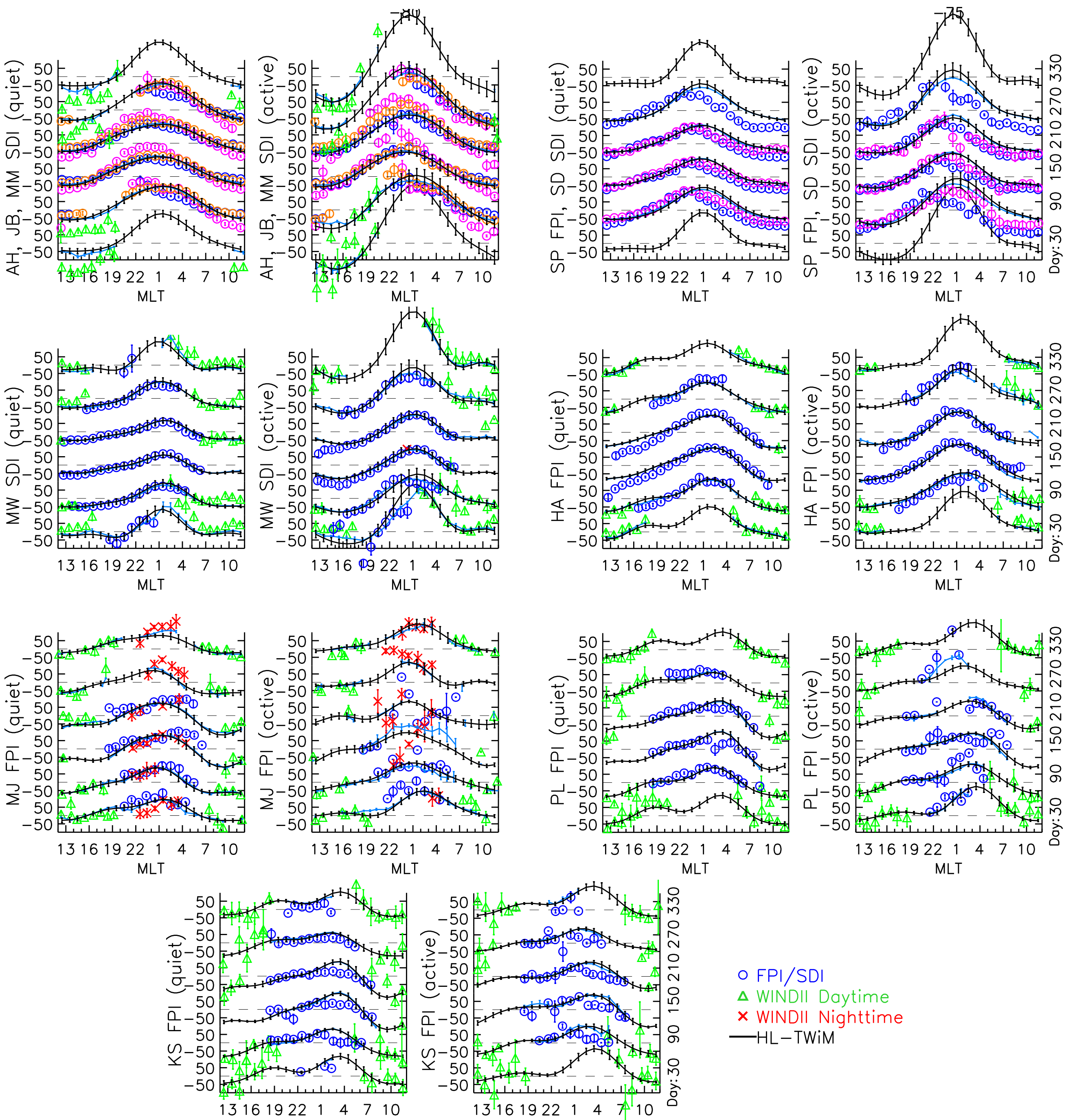
AH, JB, MM SDI (quiet)
AH, JB, MM SDI (active)
SP FPI, SD SDI (quiet)
SP FPI, SD SDI (active)
MW SDI (quiet)
MW SDI (active)
HA FPI (quiet)
HA FPI (active)
MJ FPI (quiet)
MJ FPI (active)
PL FPI (quiet)
PL FPI (active)
KS FPI (quiet)
KS FPI (active)
MLT
Day: 30 90 150 210 270 330
FPI/SDI
WINDII Daytime
WINDII Nighttime
HL-TWiM

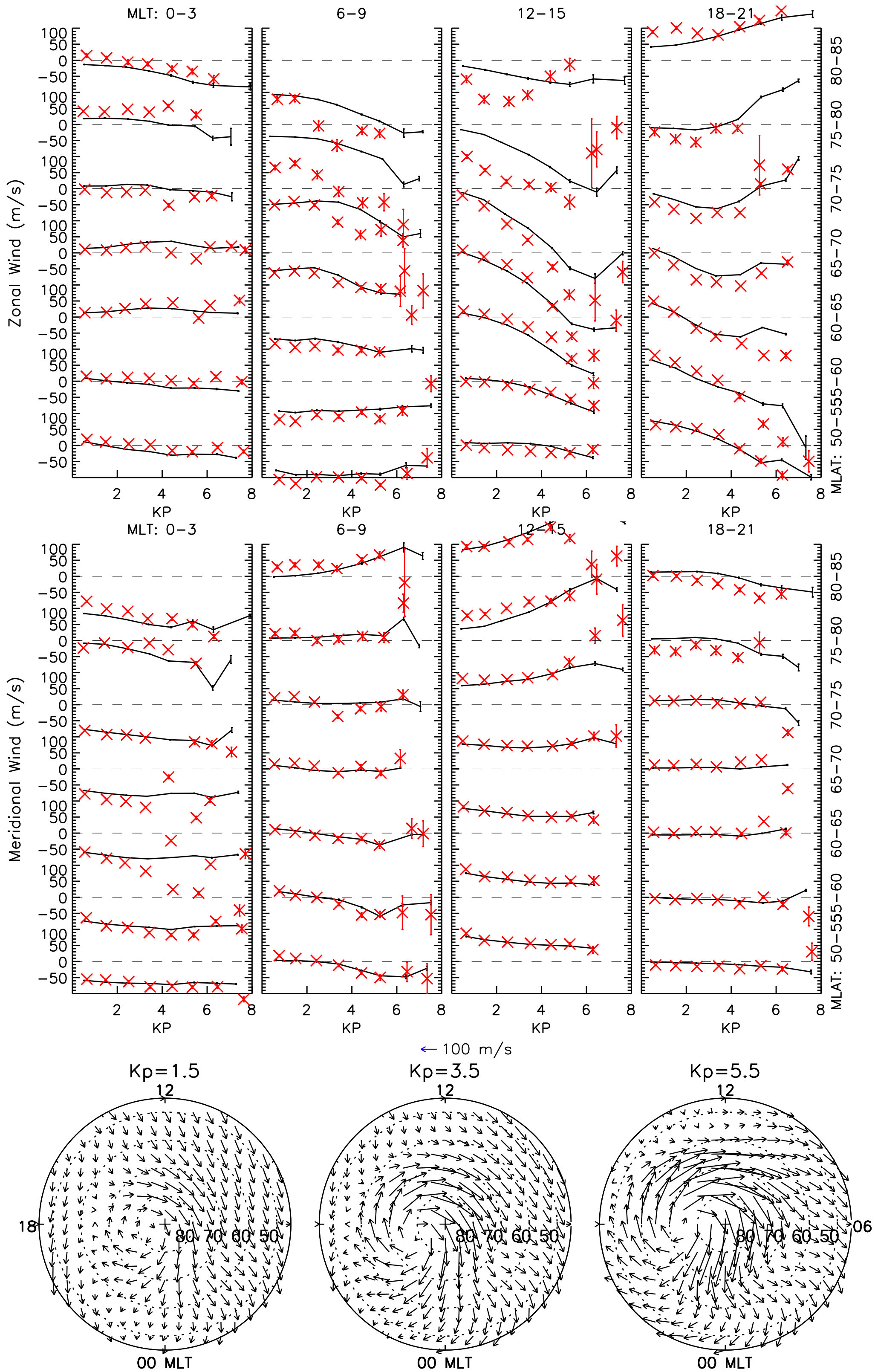

MLT: 0-3
6-9
12-15
18-21
Zonal Wind (m/s)
Meridional Wind (m/s)
KP
MLAT: 50-55
55-60
60-65
65-70
70-75
75-80
80-85
← 100 m/s
Kp=1.5
Kp=3.5
Kp=5.5
12
18
06
00 MLT
80 70 60 50

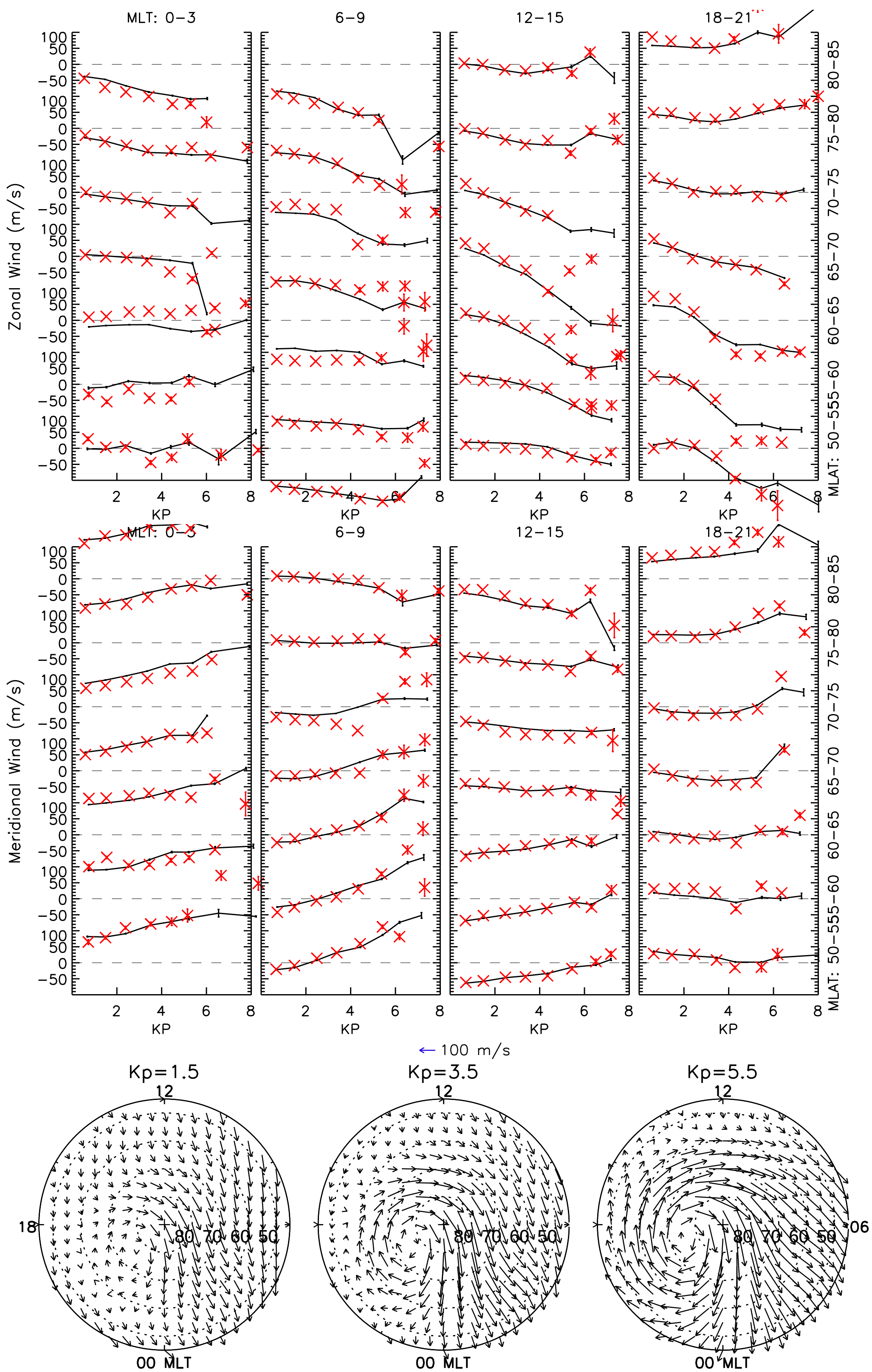
MLT: 0-3
6-9
12-15
18-21
Zonal Wind (m/s)
Meridional Wind (m/s)
KP
MLAT: 50-555-60
60-65
65-70
70-75
75-80
80-85
← 100 m/s
Kp=1.5
Kp=3.5
Kp=5.5
12
18
06
00 MLT
80 70 60 50

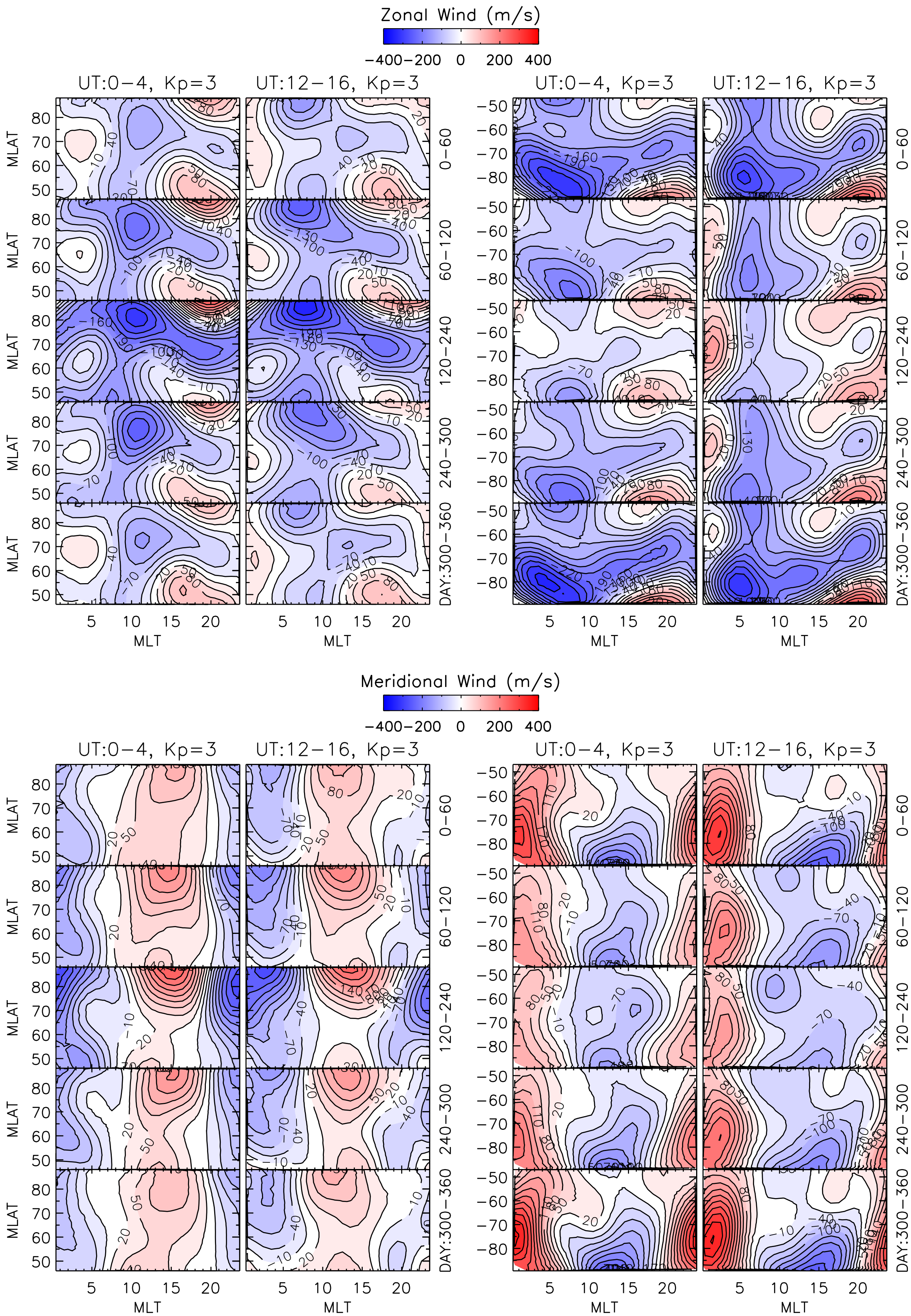

Zonal Wind (m/s)
−400 −200 0 200 400
UT:0−4, Kp=3
UT:12−16, Kp=3
MLAT
MLT
0−60
60−120
120−240
240−300
DAY:300−360
Meridional Wind (m/s)

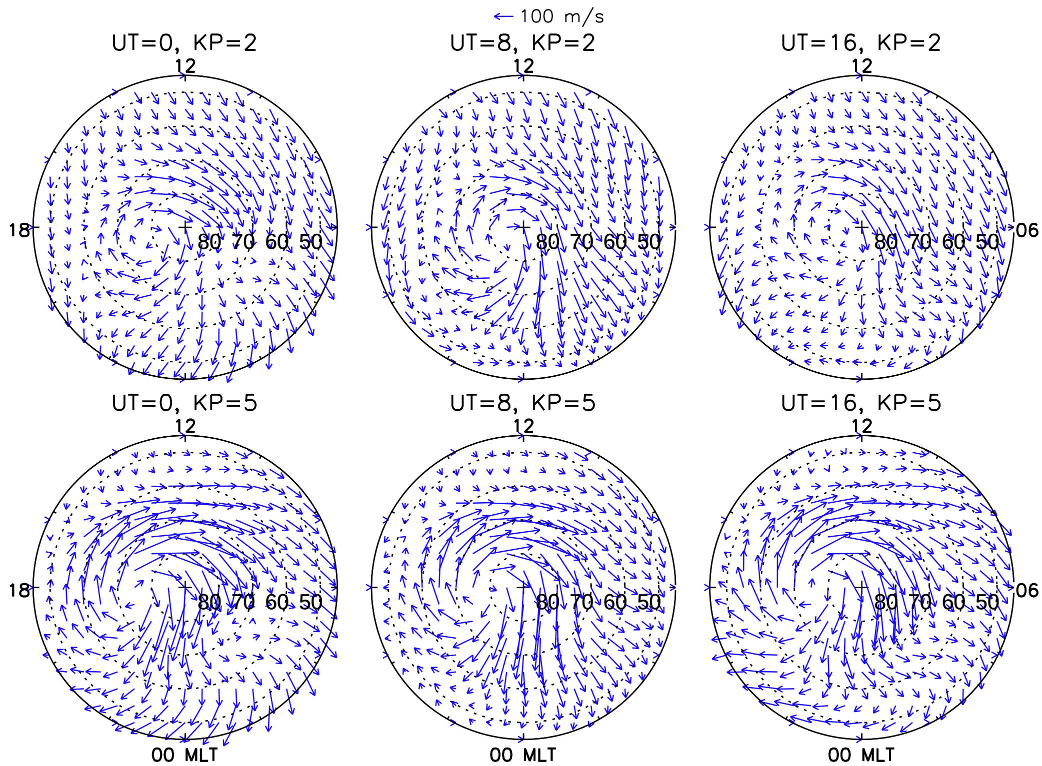
← 100 m/s
UT=0, KP=2
UT=8, KP=2
UT=16, KP=2
UT=0, KP=5
UT=8, KP=5
UT=16, KP=5
12
18
06
80 70 60 50
00 MLT

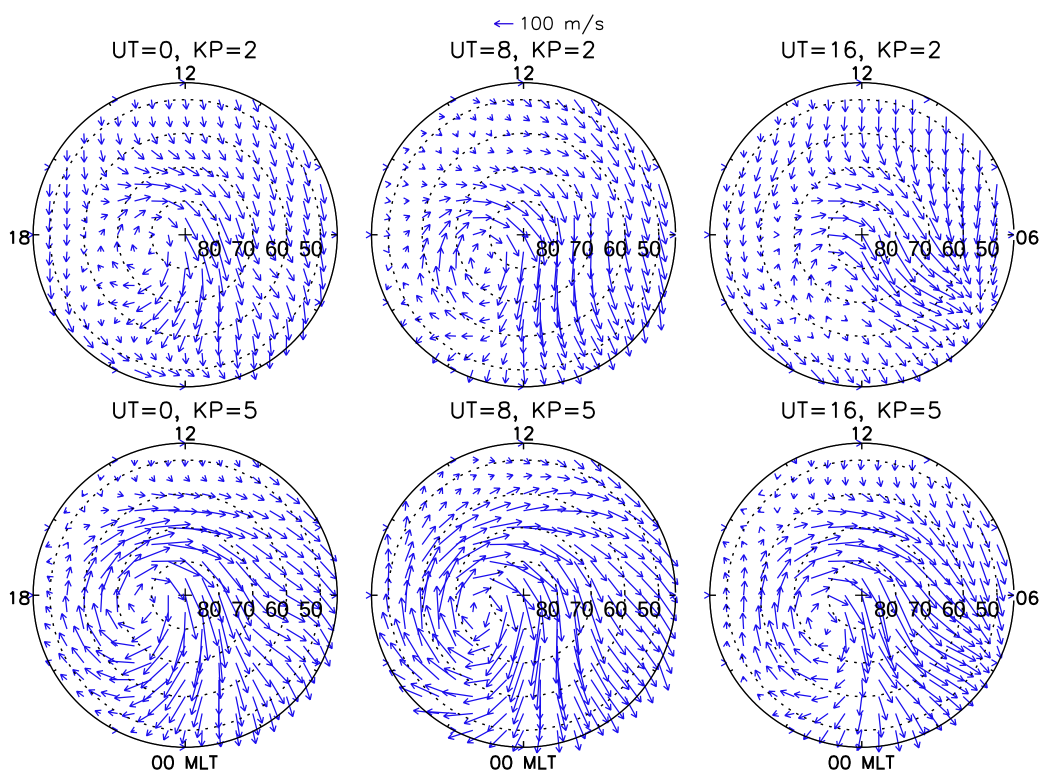
← 100 m/s
UT=0, KP=2
UT=8, KP=2
UT=16, KP=2
UT=0, KP=5
UT=8, KP=5
UT=16, KP=5
12
18
06
80 70 60 50
00 MLT

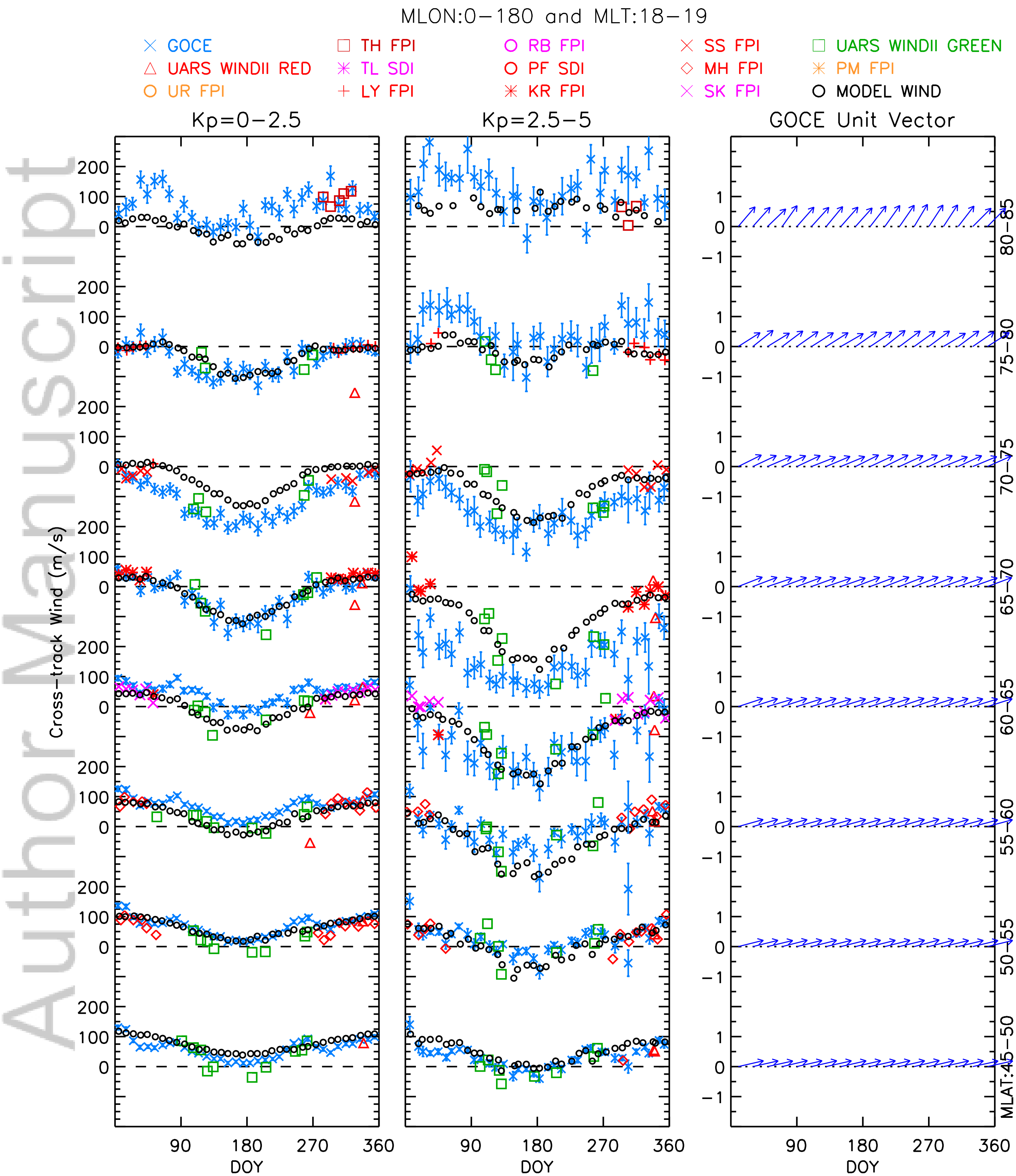

MLON:0−180 and MLT:18−19
GOCE
TH FPI
RB FPI
SS FPI
UARS WINDII GREEN
UARS WINDII RED
TL SDI
PF SDI
MH FPI
PM FPI
UR FPI
LY FPI
KR FPI
SK FPI
MODEL WIND
Kp=0−2.5
Kp=2.5−5
GOCE Unit Vector
Cross−track Wind (m/s)
DOY
80−85
75−80
70−75
65−70
60−65
55−60
50−55
MLAT:45−50

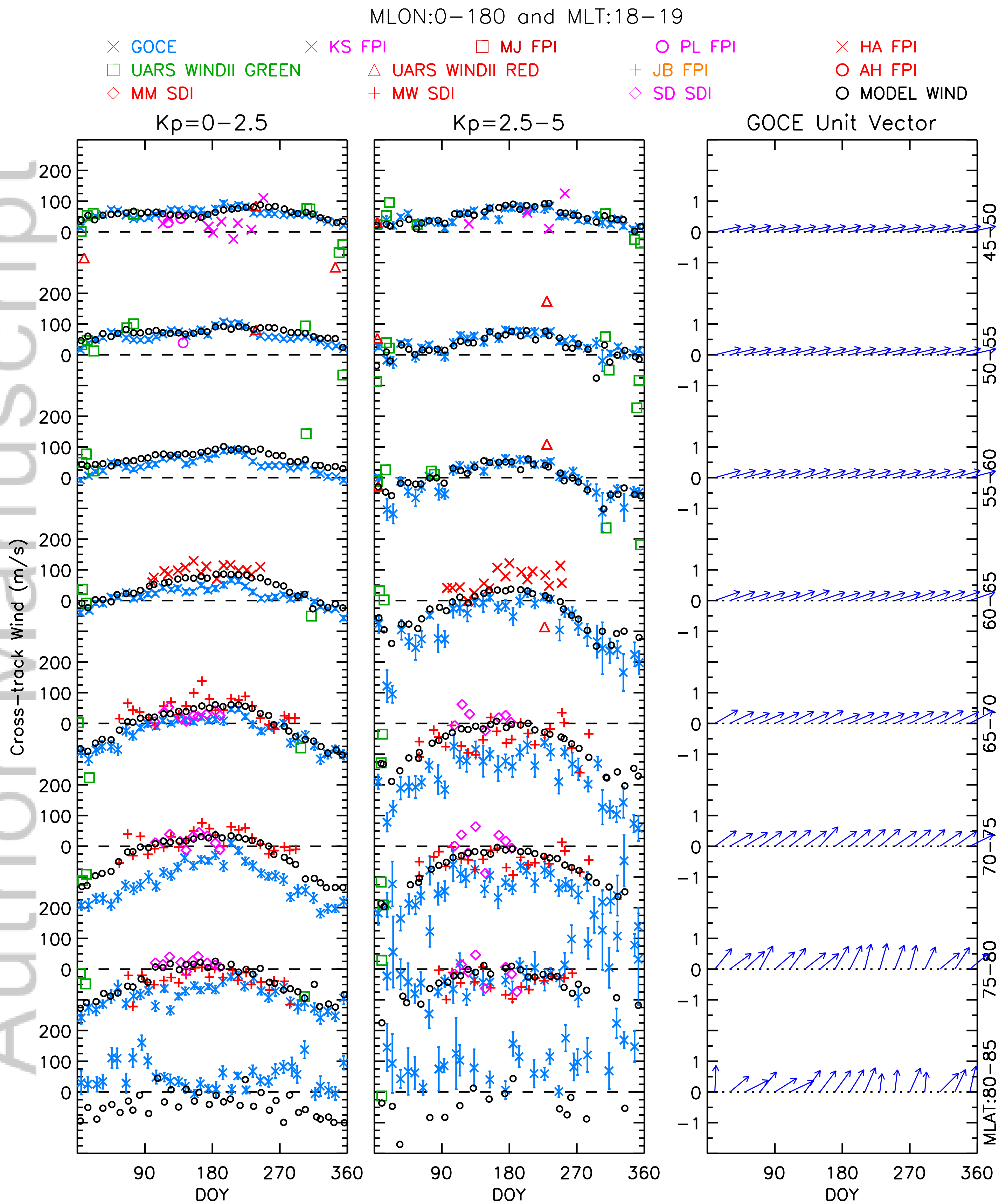

MLON:0−180 and MLT:18−19
GOCE
KS FPI
MJ FPI
PL FPI
HA FPI
UARS WINDII GREEN
UARS WINDII RED
JB FPI
AH FPI
MM SDI
MW SDI
SD SDI
MODEL WIND
Kp=0−2.5
Kp=2.5−5
GOCE Unit Vector
Cross−track Wind (m/s)
DOY
MLAT:80−85
75−80
70−75
65−70
60−65
55−60
50−55
45−50